

# Cortical Parvalbumin-Positive Interneuron Development and Function Are Altered in the APC Conditional Knockout Mouse Model of Infantile and Epileptic Spasms Syndrome

Rachael F. Ryner,<sup>1,2</sup> Isabel D. Derera,<sup>1</sup> Moritz Armbruster,<sup>1</sup> Anar Kansara,<sup>1</sup>  Mary E. Sommer,<sup>1</sup> Antonella Pirone,<sup>1</sup> Farzad Noubary,<sup>3</sup>  Michele Jacob,<sup>1</sup> and  Chris G. Dulla<sup>1</sup>

<sup>1</sup>Department of Neuroscience, Tufts University School of Medicine, Boston, Massachusetts 02111, <sup>2</sup>Cell, Molecular, and Developmental Biology Graduate Program, Tufts Graduate School of Biomedical Sciences, Boston, Massachusetts 02111, and <sup>3</sup>Department of Health Sciences, Bouvé College of Health Sciences, Northeastern University, Boston, Massachusetts 02115

Infantile and epileptic spasms syndrome (IESS) is a childhood epilepsy syndrome characterized by infantile or late-onset spasms, abnormal neonatal EEG, and epilepsy. Few treatments exist for IESS, clinical outcomes are poor, and the molecular and circuit-level etiologies of IESS are not well understood. Multiple human IESS risk genes are linked to Wnt/ $\beta$ -catenin signaling, a pathway that controls developmental transcriptional programs and promotes glutamatergic excitation via  $\beta$ -catenin's role as a synaptic scaffold. We previously showed that deleting adenomatous polyposis coli (APC), a component of the  $\beta$ -catenin destruction complex, in excitatory neurons (APC cKO mice, APC<sup>fl/fl</sup> x CaMKII $\alpha$ <sup>Cre</sup>) increased  $\beta$ -catenin levels in developing glutamatergic neurons and led to infantile behavioral spasms, abnormal neonatal EEG, and adult epilepsy. Here, we tested the hypothesis that the development of GABAergic interneurons (INs) is disrupted in APC cKO male and female mice. IN dysfunction is implicated in human IESS, is a feature of other rodent models of IESS, and may contribute to the manifestation of spasms and seizures. We found that parvalbumin-positive INs (PV<sup>+</sup> INs), an important source of cortical inhibition, were decreased in number, underwent disproportionate developmental apoptosis, and had altered dendrite morphology at P9, the peak of behavioral spasms. PV<sup>+</sup> INs received excessive excitatory input, and their intrinsic ability to fire action potentials was reduced at all time points examined (P9, P14, P60). Subsequently, GABAergic transmission onto pyramidal neurons was uniquely altered in the somatosensory cortex of APC cKO mice at all ages, with both decreased IPSC input at P14 and enhanced IPSC input at P9 and P60. These results indicate that inhibitory circuit dysfunction occurs in APC cKOs and, along with known changes in excitation, may contribute to IESS-related phenotypes.

**Key words:** cortex; development; GABA; infantile spasms; inhibition; parvalbumin interneurons

## Significance Statement

Infantile and epileptic spasms syndrome (IESS) is a devastating epilepsy with limited treatment options and poor clinical outcomes. The molecular, cellular, and circuit disruptions that cause infantile spasms and seizures are largely unknown, but inhibitory GABAergic interneuron dysfunction has been implicated in rodent models of IESS and may contribute to human IESS. Here, we use a rodent model of IESS, the APC cKO mouse, in which  $\beta$ -catenin signaling is increased in excitatory neurons. This results in altered parvalbumin-positive GABAergic interneuron development and GABAergic synaptic dysfunction throughout life, showing that pathology arising in excitatory neurons can initiate long-term interneuron dysfunction. Our findings further implicate GABAergic dysfunction in IESS, even when pathology is initiated in other neuronal types.

Received Mar. 18, 2022; revised Nov. 14, 2022; accepted Dec. 22, 2022.

Author contributions: R.F.R., I.D.D., M.A., A.P., M.J., and C.G.D. designed research; R.F.R., I.D.D., M.A., and M.E.S. performed research; R.F.R., I.D.D., M.A., A.K., and F.N. analyzed data; R.F.R. and I.D.D. wrote the first draft of the paper; R.F.R., I.D.D., M.A., A.P., M.J., and C.G.D. edited the paper; R.F.R. and C.G.D. wrote the paper.

This work was supported by R01 NS100706 to C.G.D., R56 NS094889 to C.G.D., CURE Epilepsy to C.G.D. and M.J., and American Epilepsy Society Predoctoral Fellowship to R.F.R. We thank members of the C.G.D. laboratory, the M.J. laboratory, Oliva Drake, and Elisabeth Lawton for helpful discussions.

The authors declare no competing financial interests.

Correspondence should be addressed to Chris G. Dulla at Chris.Dulla@tufts.edu.

<https://doi.org/10.1523/JNEUROSCI.0572-22.2022>

Copyright © 2023 the authors

## Introduction

Infantile and epileptic spasms syndrome (IESS) is a devastating developmental epilepsy syndrome that occurs in the first year of life (West, 1841; Pavone et al., 2014) and is characterized by flexion/extension spasms, neurodevelopmental delays, and hypsarrhythmia (Paciorkowski et al., 2011; Michaud et al., 2014; Boutry-Kryza et al., 2015; Pirone et al., 2017). Early suppression of spasms and epileptiform activity can improve clinical outcomes (Shields, 2006; El Achkar and Spence, 2015), but available therapies are not widely effective and have adverse effects (Go et al., 2012; Riikonen

et al., 2015). The pathologic processes that lead to IESS are not well defined, but inhibitory GABAergic network dysfunction is implicated across multiple IESS mouse models (Price et al., 2009; Marsh et al., 2009, 2016; Olivetti et al., 2014; Katsarou et al., 2018). In addition, GABAergic dysfunction is seen in a mouse model of tuberous sclerosis complex (TSC) (Fu et al., 2012), which in humans is associated with IESS (TSC mouse models have not been demonstrated to have spasms). Finally, GABAergic dysfunction occurs in human neurologic disorders associated with IESS, some of which may be considered “interneuronopathies” (Bonneau et al., 2002; Kato and Dobyns 2005). Understanding the mechanisms that lead to synaptic, cellular, and circuit dysfunction in IESS, and what changes underlie spasms and seizures on a circuit-level, is essential to developing novel therapeutic interventions.

Interestingly, several genes linked to IESS, including *Arx*, *LISI*, *FOXG1*, and *TSC1/2* (Stromme et al., 2002a,b; Paciorkowski et al., 2011; Striano et al., 2011; Michaud et al., 2014), associate with the  $\beta$ -catenin signaling pathway.  $\beta$ -catenin is strongly implicated in neurodevelopmental disorders (Cotter et al., 1998; Zhang et al., 1998; Mohn et al., 2014; Kuechler et al., 2015; Wickham et al., 2019; Alexander et al., 2020) and plays a dual role in (1) mediating transcriptional activation of Wnt-target genes (Behrens et al., 1996; Molenaar et al., 1996) and (2) as a structural element stabilizing synapses via its interactions with classic cadherins (Bamji et al., 2003; Kiryushko et al., 2004; Schlessinger et al., 2009; Salinas, 2012; Viturera et al., 2012). *Arx* is expressed in GABAergic interneurons (INs) (Colombo et al., 2004; Poirier et al., 2004; Friocourt et al., 2006) and binds to  $\beta$ -catenin to positively regulate downstream signaling (Cho et al., 2017). The adenomatous polyposis coli (APC) protein, part of the  $\beta$ -catenin destruction complex, associates with *FOXG1* and *LISI*, regulating Wnt signaling and directing cell fate in the developing brain (Kato and Dobyns, 2003; McManus et al., 2004; Hebbar et al., 2008; Danesin et al., 2009; Ivaniutsin et al., 2009; Miyoshi and Fishell, 2012). *TSC1/2* functions as a repressor of  $\beta$ -catenin, and conditional deletion of *TSC1/2* in GABAergic IN progenitors decreases seizure threshold (Mak et al., 2005; J. Huang and Manning, 2008; Carson et al., 2013). Although these data provide correlative evidence linking IESS to APC/Wnt/ $\beta$ -catenin signaling, there are few studies that directly link the two.

To determine the link between  $\beta$ -catenin and IESS, we used APC conditional homozygous KO mice (APC<sup>fl/fl</sup> crossed with CaMKII $\alpha$ <sup>CRE</sup>/APC<sup>fl/+</sup>, APC cKO), which lack APC in excitatory forebrain neurons beginning in early postnatal life, leading to elevated levels of  $\beta$ -catenin protein (Mohn et al., 2014). APC cKO mice recapitulate phenotypes relevant to human IESS, including infantile flexion/extension spasms, abnormal neonatal EEG activity, and spontaneous electroclinical seizure activity in adult mice (Pirone et al., 2017). APC cKO mice also show intellectual disabilities and behavioral abnormalities considered relevant to human autism spectrum disorder (Mohn et al., 2014), which are often comorbid with IESS (El Achkar and Spence, 2015). Consistent with  $\beta$ -catenin's role in synapse density and maturation, APC cKO mice show increased immature spine density and enhanced excitatory neurotransmission in the hippocampus and cortex as early as postnatal day 9 (P9), the same developmental time point of peak behavioral spasms in this model. Cortical circuit maturation is activity-dependent; therefore, aberrant excitation in early life could drive long-term changes in brain function and lead to adult seizures. Of particular interest, the survival and maturation of GABAergic

INs are dynamically regulated by excitatory activity during early development (Southwell et al., 2012; Priya et al., 2018; Wong et al., 2018). GABAergic INs provide inhibitory constraint of cortical circuits and are critical in developmental cortical circuit refinement (Freund and Buzsáki, 1998; Buzsáki, 2006; Klausberger and Somogyi, 2008), and GABAergic circuit dysfunction is implicated in epilepsy and IESS (F. H. Yu et al., 2006; Price et al., 2009; Khazipov, 2016). Interestingly, parvalbumin-positive (PV<sup>+</sup>) IN density has been reported to be decreased in the adult PFC of APC cKO mice (Pirone et al., 2018), but the mechanisms by which PV<sup>+</sup> IN density decreases and how this affects inhibitory synaptic function are unknown.

We hypothesized that GABAergic IN survival and maturation may be altered in the APC cKO mouse model of IESS.  $\beta$ -catenin regulates both cortical excitation (Bamji et al., 2003; Wisniewska et al., 2012) and GABAergic IN development (Gulacsi and Anderson, 2008), providing rationale to suspect that GABAergic IN maturation may be disrupted in the APC cKO model of IESS. Here we used genetic, anatomic, and electrophysiological approaches to show that PV<sup>+</sup> INs, an important source of cortical inhibition, are reduced in number, undergo increased levels of developmental apoptosis, and receive excessive excitation in the somatosensory cortex (SSC) of neonatal APC cKO mice. Consistent with early life excitation driving long-term changes in GABAergic IN function, adult APC cKOs show altered GABAergic synaptic transmission onto excitatory cortical neurons and PV<sup>+</sup> IN intrinsic excitability. Overall, our study shows that loss of APC in excitatory forebrain neurons can disrupt the maturation and function of GABAergic networks and, along with changes in excitatory neurons, may contribute to IESS-relevant phenotypes.

## Materials and Methods

**Animals.** APC cKO mice of both sexes were generated as previously described (Mohn et al., 2014). Briefly, APC was conditionally deleted by crossing male mice homozygous for the floxed APC allele (APC<sup>fl/fl</sup>) with female mice that are heterozygous for the floxed APC allele (APC<sup>fl/+</sup>) and express Cre-recombinase under the control of the CaMKII $\alpha$  promoter (CaMKII $\alpha$ Cre). APC<sup>fl/fl</sup> mice are on a mixed FVB and C57B6J background. CamKII $\alpha$  mice are on a mixed C57B6/J and 129S1/SvImj background. This generates homozygous APC cKO mice (APC<sup>fl/fl</sup>/Cre<sup>+</sup>), mice heterozygous for APC in excitatory neurons (APC<sup>fl/+</sup>/Cre<sup>+</sup>), and WT mice (APC<sup>fl/fl</sup>/Cre<sup>-</sup>, APC<sup>fl/+</sup>/Cre<sup>-</sup>). Only homozygous cKO mice and WT mice are used in this study. To identify PV<sup>+</sup> cortical INs (PV<sup>+</sup> INs), we also integrated GAD67-eGFP (G42) mice (CB6F1/J background), in which a subset of PV<sup>+</sup> INs are labeled with green fluorescent protein (GFP<sup>+</sup>) (Chattopadhyaya et al., 2004; Hanson et al., 2019) (JAX stock #007677), into our APC cKO breeding strategy to generate triple-transgenic mice. Finally, to identify both PV<sup>+</sup> and somatostatin-positive (SST<sup>+</sup>) INs, Lhx6-GFP mice (FVB/NTac background) were also used (Tg(Lhx6-EGFP)BP221Gsat/Mmmh, RRID:MMRRC\_000246-MU), which express GFP in medial ganglionic eminence (MGE)-derived neurons. Triple-transgenic mice were generated that were APC cKO or WT (as above) but also contained the Lhx6-GFP gene. Cre-negative and non-APC floxed littermates were used as controls. As above, in both G42-GFP and Lhx6-GFP experiments, all APC cKO mice were homozygous KOs. All procedures were approved by the Tufts University Institutional Animal Care and Use Committee. Because of the complexity of the genetic manipulations used, animals were not balanced by sex, but any available animals of the appropriate genotype were used. Experimenters were blinded to genotype until after data analysis was completed.

**Brain slice preparation.** Somatosensory cortical brain slices (400  $\mu$ m) were prepared from P9, P14, and >P60 APC cKO mice or WT littermates as previously described (Cantu et al., 2015; Hanson et al., 2015,

2019; Pirone et al., 2017; Koenig et al., 2019). Mice were anesthetized with isoflurane, decapitated, and brains were rapidly removed and placed in ice-cold cutting solution consisting of the following (in mM): 234 sucrose, 11 glucose, 24 NaHCO<sub>3</sub>, 2.5 KCl, 1.25 NaH<sub>2</sub>PO<sub>4</sub>, 10 MgSO<sub>4</sub>, and 0.5 CaCl<sub>2</sub>. Cutting solution was constantly oxygenated with a mixture of 95% O<sub>2</sub>:5% CO<sub>2</sub>. The brain was glued to the slicing stage of Vibratome 3000 sectioning system (Leica), and slices were cut in a coronal orientation. The slices were then incubated in 32°C oxygenated aCSF consisting of the following (in mM): 126 NaCl, 2.5 KCl, 1.25 NaH<sub>2</sub>PO<sub>4</sub>, 1 MgSO<sub>4</sub>, 2 CaCl<sub>2</sub>, 10 glucose, 26 NaHCO<sub>3</sub> for 1 h. Slices were then allowed to cool to room temperature and used for electrophysiological experiments.

**Whole-cell patch-clamp recordings.** Slices were placed in the recording chamber of an Olympus BX51 microscope with continuous superfusion of oxygenated aCSF maintained at 32°C, as previously described (Cantu et al., 2015; Hanson et al., 2015, 2019; Pirone et al., 2017; Koenig et al., 2019). Layer 5 pyramidal neurons and G42-GFP<sup>+</sup> INs were identified using a 60× water immersion objective with epifluorescence (Olympus). Electrophysiological signals were obtained using a Multiclamp 700B amplifier (Molecular Devices), low pass filtered at 1 kHz, and digitized at 20 kHz. Data were recorded onto a computer (Digidata 1440A, Molecular Devices) using pClamp software (Molecular Devices). Recording pipettes were pulled from borosilicate glass (3–5 MΩ, Sutter Instruments). For voltage-clamp recordings, a CsMs-based internal solution was used containing the following (in mM): 140 CsMs, 10 HEPES, 5 NaCl, 0.2 EGTA, 5 QX314, 1.8 MgATP, 0.3 NaGTP. To isolate spontaneous EPSCs (sEPSCs) and miniature EPSCs (mEPSCs), cells were voltage-clamped at a holding potential of –60 mV. To isolate spontaneous IPSCs (sIPSCs) and miniature IPSCs (mIPSCs), cells were voltage-clamped at a holding potential of 0 mV. Glutamate receptor antagonists (DNQX [20 μM] and CPP [10 μM]) were included in the aCSF for IPSC recordings. mEPSCs/IPSC/mIPSCs were recorded in the presence of 1 μM TTX (Abcam). For current-clamp recordings, internal solution contained the following (in mM): 130 K-gluconate, 10 HEPES, 5 KCl, 5 EGTA, 2 NaCl, 1 MgCl<sub>2</sub>, and 1.8 MgATP, 0.3 NaGTP. In current-clamp recordings, glutamate and GABA receptor antagonists (DNQX [20 μM], CPP [10 μM], and gabazine [10 μM]) were included in the aCSF to block synaptic activity. Current injection steps were applied ranging from –200 to 400 pA in 10 or 20 pA steps. Access resistance was monitored throughout whole-cell recordings, and electrophysiology data were not further analyzed if the access resistance changed by >20%. For sEPSCs/sIPSCs and mEPSCs/mIPSCs, 2 min recording segments were analyzed using MiniAnalysis (Synaptosoft), and average frequency and amplitude were quantified. Cumulative probability distributions were calculated by taking 100 randomly sampled events from each recorded cell and then pooling the randomly sampled data across cells in each condition.

**IN filling and reconstruction.** To reconstruct IN dendrites, recording pipettes were filled with an internal recording solution that contained 0.2% biocytin. Current injections from –200 to 400 pA were injected in 10 pA intervals to facilitate cell filling. Then the patch pipette was slowly withdrawn from the cell, forming an outside-out patch, allowing the cell to reseal. Sections were incubated in oxygenated aCSF for at least 15 min and then placed in 4% PFA for 24 h. After PFA fixation, sections were washed 4× in PBS and then incubated overnight in 2% BSA, 10% goat serum, 0.1% Triton X-100, and 1:50 streptavidin Cy3 (Invitrogen). The next day, sections were washed 4× in PBS, followed by 50% glycerol:PBS and 90% glycerol:PBS, for 30 min each. Slices were mounted with Fluoromount-G (Southern Biotechnology). Filled cells were imaged on an AIR confocal microscope (Nikon) with a 20× objective (Nikon). Z stacks were taken of the cells, in 1 μm increments, to include all visible cellular processes. Three-dimensional reconstructions of dendrites and Sholl analyses were done using Imaris (Bitplane).

**G42-GFP, Lhx6-GFP, and Cl-Caspase 3 cell counts.** Animals (P3, P5, P7, P9, P14, and >P60) were transcardially perfused with PBS followed by 4% PFA in 0.4 M PB. Brains were dissected and postfixed in PFA for 24 h, then cryopreserved in 30% sucrose solution for a minimum of 3 d. Cortical brain sections (40 μm) were collected using a cryostat (Microm, Thermo Scientific), and free-floating sections were blocked

in 10% goat serum (GS), 5% BSA, and 0.2% Tween 20-PBS (PBST). Sections were immunolabeled with primary antibodies against GFP (1:1000; Abcam ab13970), PV (1:2500; Swant McAB 235), SST (1:100; Millipore MAB354), and cleaved caspase 3 (1:500; Cell Signaling Technology Asp175 D3E9) in 5% GS, 1% BSA, and 0.2% PBST. All secondary antibodies were used at a ratio of 1:500 in 5% GS, 1% BSA, and 0.2% PBST (anti-chicken-GFP, Abcam ab6873; anti-mouse-Cy3, Jackson ImmunoResearch Laboratories 115-165-003; anti-rat-AlexaFluor-647, Jackson ImmunoResearch Laboratories 112-605-167; anti-rabbit-AlexaFluor-594, Invitrogen). Images were collected for cell counting using a Keyence epifluorescence microscope from a single plane of focus per section. Composite images of whole cortex were made using 10× objective. Illumination power and exposure were set to optimize cell body visualization and kept consistent across age and genotype. Using this imaging modality, all cells in the plane of focus were quantified. ROIs were drawn using ImageJ software (National Institutes of Health) in primary SSC, primary motor cortex, and infralimbic and prelimbic areas combined for PFC, and cell numbers were counted within the ROI. The somatosensory, motor, and prefrontal (infralimbic and prelimbic areas) cortex was identified using the Allen Mouse Brain Atlas (<https://mouse.brain-map.org/static/atlas>). Cells within the somatosensory, motor, and PFC were counted from the pial surface to the white matter underlying the cortex. To define the medial/lateral boundary of the ROI, we again consulted the Allen Mouse Brain Atlas to define a rectangular region safely within the anatomic borders of each region. For SSC, this region was directly above the lateral portion of the hippocampus, for motor cortex, this region was directly above the medial portion of the hippocampus, for the PFC, the medial cortex before the corpus callosum crosses for the PFC was used. The ROI size was ~500,000–600,000 μm<sup>2</sup> for all regions. There was no difference in the size of the ROI used to quantify cell density in WT compared with cKO. As brain size for P9 mice is smaller than adults, the ROI width was increased to ensure consistent ROI size across all age groups. Cells were identified based on epifluorescence and cellular morphology of the cell body. A range of 2–5 sections, with one ROI per section, were used per animal. All the resulting densities from these ROIs were used in linear mixed-model statistical analysis, while the average of all densities from 1 animal was used in *t* test statistical analysis. GFP<sup>+</sup>, PV<sup>+</sup>, and SST<sup>+</sup> cell densities were calculated by dividing the number of cells by the area of the quantified ROI. Laminar density ratios were calculated by dividing superficial cortical layer densities (layers 2/3) by deep cortical layer densities (layers 4, 5/6). Cl-caspase 3 ratios were calculated by dividing the number of G42-GFP/Cl-casp<sup>+</sup> cells by total G42-GFP<sup>+</sup> cells in the ROI. Putative PV<sup>+</sup> IN density in the Lhx6-GFP background (Lhx6-GFP<sup>+</sup>/SST<sup>+</sup>) was calculated by subtracting Lhx6-GFP<sup>+</sup>/SST<sup>+</sup> IN density from total Lhx6-GFP<sup>+</sup> density.

**Statistical analysis.** At least 3 animals of each genotype and age were used per experiment. *N* values for each experiment are included in the figure legends. The normality of all data was tested using Shapiro–Wilk test. Student's two-sample *t* test was used to compare WT and cKO mice in normally distributed data. Wilcoxon rank-sum test was used in non-normally distributed data. Both sexes were included in all experiments. At P9 and P14, animal sex was not recorded. For P60 immunolabeling and IPSC recording, sex was evaluated as a biological variable for all data collected. Because most measures did not show an effect of sex as a biological variable, the challenges of sex-balancing studies using triple-transgenic mice, and previous data showing no difference in spasm and seizure phenotypes between males and females (Mohn et al., 2014; Pirone et al., 2017), we pooled male and female data at all time points. This caveat is noted in the Discussion. Outliers were not excluded in any datasets. For all experiments, except synaptic recording cumulative distribution analysis,  $\alpha = 0.05$ . Averages of multiple measurements from the same animal were used in *t* tests and rank-sum tests. To analyze the cumulative distribution plots of synaptic recordings, MATLAB was used to randomly sample 100 interevent intervals (IEIs) and amplitudes per cell recording to generate distributions. A Kolmogorov–Smirnov (K-S) test was used to compare the distribution between genotypes. Alpha for K-S tests was set to 0.00001 based on a 5% false positive rate when

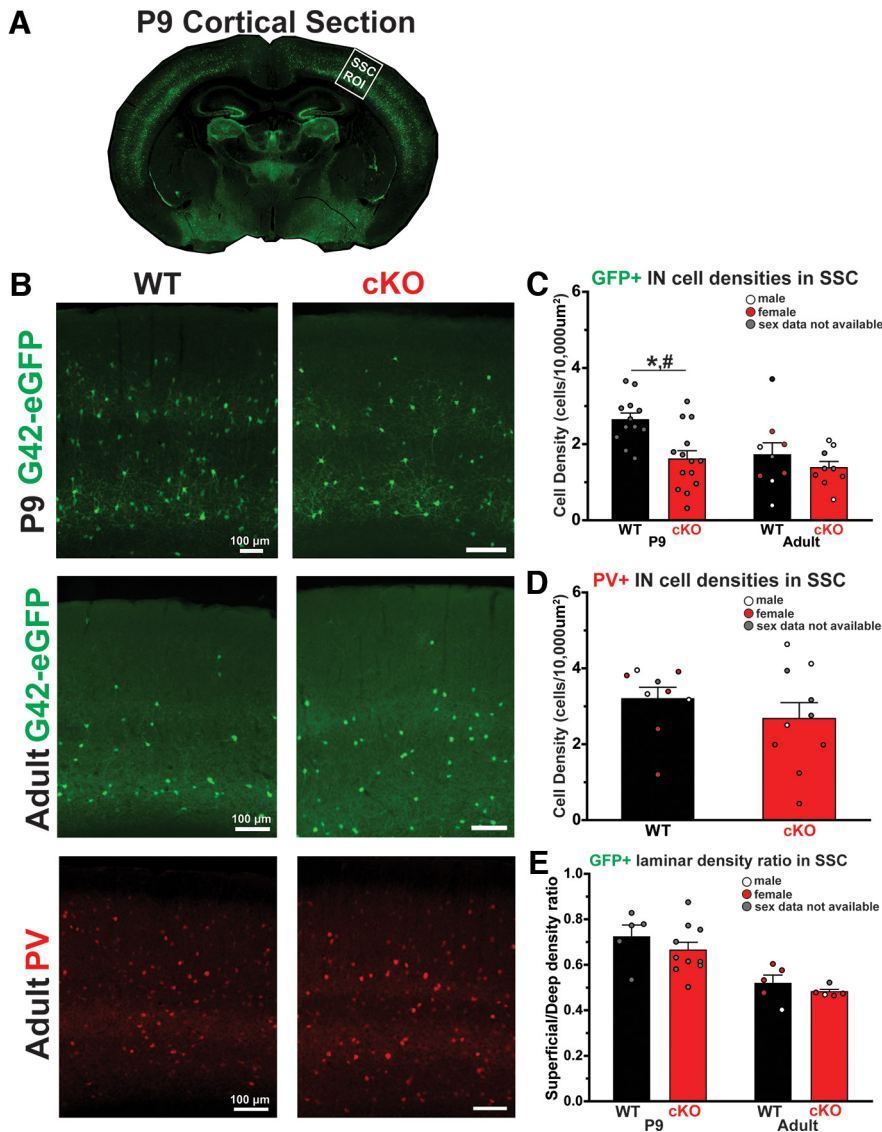


**Figure 1.** Immature PV<sup>+</sup> IN density, as measured using G42-GFP mice, is reduced in the SSC of APC cKO mice at P9. **A**, Example ROI drawn in primary SSC of a P9 mouse brain section. **B**, Representative fluorescent images in SSC of G42-GFP<sup>+</sup> (green, labeling a subset of PV<sup>+</sup> INs) cells at (top) P9 and (middle) adult (>P60) and (bottom) PV<sup>+</sup> immunolabeled (red) cells in adult for WT and cKO mice. Scale bar, 100 µm. **C**, Bar graph of average G42-GFP<sup>+</sup> IN cell density per animal at P9 for WT (black bar, *n* = 12 animals) and cKO (red bar, *n* = 14 animals) mice (*p* = 1.60e-3, *t*<sub>(24)</sub> = 3.56, two-sample *t* test; *p* = 9.86e-4, *t*<sub>(61)</sub> = 3.70, LMM) and adult WT (*n* = 9 animals) and cKO (*n* = 9 animals; *p* = 0.36, *t*<sub>(16)</sub> = 0.95, two-sample *t* test; *p* = 0.27, *t*<sub>(39)</sub> = 1.13, LMM). **D**, Bar graph of average PV<sup>+</sup> IN densities per animal in adult for WT (black bar, *n* = 9 animals) and cKO (red bar, *n* = 10 animals) mice (*p* = 0.33, *t*<sub>(17)</sub> = 1.00, two-sample *t* test; *p* = 0.92, *t*<sub>(23)</sub> = 0.11, LMM). **E**, Bar graph of the laminar density ratio, which represents the ratio of superficial layer densities to deep layer densities, of G42-GFP<sup>+</sup> INs at P9 in WT (black bar, *n* = 5 animals) and cKO (red bar, *n* = 10 animals) mice (*p* = 0.35, *t*<sub>(13)</sub> = 0.96, two-sample *t* test; *p* = 0.21, *t*<sub>(39)</sub> = 1.32, LMM) and adult WT (*n* = 5 animals) and cKO (*n* = 5 animals; *p* = 0.36, *t*<sub>(8)</sub> = 0.98, two-sample *t* test; *p* = 0.33, *t*<sub>(19)</sub> = 1.01, LMM). \**p* < 0.05, two-sample *t* test. #*p* < 0.05, LMM, effect of genotype. Each data point represents the average ratio for 1 animal. Symbol interior color represents sex data. Error bars indicate SEM.

resampling the same control datasets. For all experiments, we also performed linear mixed-effects modeling (LMM) on the same dataset to determine statistical significance while accounting for sources of both intra- and inter-animal variability (Aarts et al., 2014; Boisgontier and Cheval, 2016; Lau et al., 2017; Hanson et al., 2019; Koenig et al., 2019; Z. Yu et al., 2022). LMM utilizes all measurements taken from the same animal while accounting for both intra- and inter-animal variability through the use of fixed and random effects. Fixed effects in our models included terms for genotype and interaction of genotype with another measure (i.e., current injection amplitude). Random effects in our models included terms to capture the dependency in data from the same cell/tissue and the same mouse. Example code used in RStudio (version 1.2.5033) for running LMM using lme4,

lmeRtest, matrix, and stats packages on P9 current injections (see Fig. 11) was as follows:

```
>currentinjectionP9=lmer (APs ~ current_step*genotype + (1|mouse) + (1|mouse:cell), data = currentinjectionP9_LMM, na.action = "na.omit," REML=FALSE)
```

In this example code from RStudio, a dataset (which we labeled “currentinjectionP9\_LMM” in RStudio) was used to analyze the effect of genotype and current step (“current\_step\*genotype”) on action potential number (“APs”), and in which the inter-animal (“1|mouse”) and intra-animal (“1|mouse:cell”) variability was considered. For LMM, *t* values >1.96 and <-1.96 were considered to be statistically significant.

## Results

### Immature PV<sup>+</sup> IN cell density is altered in APC cKO mice using G42 GAD67-eGFP mice

To investigate IN numbers in the developing APC cKO SSC, we quantified the density of PV<sup>+</sup> and SST<sup>+</sup> INs, MGE-derived inhibitory cells that together make up 60% of cortical GABAergic INs. Because PV protein is not expressed until approximately P12-P14 in the cerebral cortex (Solbach and Celio, 1991; de Lecea et al., 1995), we used two different genetic approaches to identify immature PV<sup>+</sup> INs, GAD67-GFP and Lhx6-GFP reporter lines. APC cKO mice were crossed with G42 mice (GAD67-eGFP), which have a GFP expression cassette inserted under the control of the GAD67 promoter (Chattopadhyaya et al., 2004). Multiple studies confirm that a subset of PV<sup>+</sup> INs express GFP as early as P3 in G42 mice, well before the expression of PV protein (Chattopadhyaya et al., 2004; Southwell et al., 2012; Hanson et al., 2019). G42-GFP<sup>+</sup>, PV<sup>+</sup>, and SST<sup>+</sup> cells were quantified in the SSC at P9 and in adult (>P60) mice. G42-GFP<sup>+</sup> IN cell density was significantly lower at P9 in the cKO mice (1.61 ± 0.22 cells/10,000 µm<sup>2</sup>) compared with WT littermates (2.64 ± 0.18 cells/10,000 µm<sup>2</sup>; Fig. 1B,C). No immunohistochemical labeling of PV<sup>+</sup> INs was seen in either genotype at P9, consistent with lack of PV expression at this age (data not shown). SST<sup>+</sup> IN density was similar between P9 APC cKO (2.39 ± 0.34 cells/10,000 µm<sup>2</sup>) and WT (2.75 ± 0.57 cells/10,000 µm<sup>2</sup>) mice (Fig. 2A,B).

In adult mice, there was no significant difference in the density of G42-GFP<sup>+</sup> cells (cKO density 1.38 ± 0.17 cells/10,000 µm<sup>2</sup>; WT density 1.72 ± 0.32 cells/10,000 µm<sup>2</sup>; Fig. 1B,C), PV<sup>+</sup> immunolabeled INs (cKO density 2.68 ± 0.42 cells/10,000 µm<sup>2</sup>; WT density 3.20 ± 0.30 cells/10,000 µm<sup>2</sup>; Fig. 1B,D), or SST<sup>+</sup> INs (cKO density 2.67 ± 0.90 cells/10,000 µm<sup>2</sup>; WT density 2.37 ± 0.57 cells/10,000 µm<sup>2</sup>; Fig. 2A,B) between APC cKO and WT mice. The laminar density between superficial (layers 2/3)

and deep (layers 4, 5/6) cortical layers did not differ for G42-GFP<sup>+</sup> INs at P9 (cKO ratio  $0.66 \pm 0.03$ ; WT ratio  $0.72 \pm 0.05$ ) or adult (cKO ratio  $0.48 \pm 0.01$ ; WT ratio  $0.52 \pm 0.04$ ; Fig. 1E). The laminar distribution of SST<sup>+</sup> INs was also not altered (P9: cKO ratio  $0.44 \pm 0.06$ ; WT ratio  $0.36 \pm 0.11$ ; adult: cKO ratio  $0.78 \pm 0.13$ ; WT ratio  $0.77 \pm 0.06$ ; Fig. 2C). To determine whether similar reductions in G42-GFP<sup>+</sup> INs were seen in other regions, we also examined motor (MC) and PFC in P9 and adult mice (Fig. 3). In APC cKO mice, G42-GFP<sup>+</sup> IN density was decreased at P9, but not adults in the MC (P9: WT  $1.95 \pm 0.15$  cells/10,000  $\mu\text{m}^2$ , cKO  $1.14 \pm 0.14$  cells/10,000  $\mu\text{m}^2$ ; adult: WT  $1.62 \pm 0.27$  cells/10,000  $\mu\text{m}^2$ , cKO  $1.13 \pm 0.17$  cells/10,000  $\mu\text{m}^2$ , Fig. 3A) and PFC (P9: WT  $1.26 \pm 0.14$  cells/10,000  $\mu\text{m}^2$ , cKO  $0.77 \pm 0.12$  cells/10,000  $\mu\text{m}^2$ ; adult: WT  $1.13 \pm 0.26$  cells/10,000  $\mu\text{m}^2$ , cKO  $0.61 \pm 0.09$  cells/10,000  $\mu\text{m}^2$ , Fig. 3D), similar to what we report in SSC. At P9, SST<sup>+</sup> IN density was similar in WT and APC cKO mice in both MC (WT  $3.42 \pm 0.67$  cells/10,000  $\mu\text{m}^2$ , cKO  $2.81 \pm 0.36$  cells/10,000  $\mu\text{m}^2$ , Fig. 3C) and PFC (WT  $1.67 \pm 0.32$  cells/10,000  $\mu\text{m}^2$ , cKO  $2.52 \pm 0.79$  cells/10,000  $\mu\text{m}^2$ , Fig. 3F) PV<sup>+</sup> IN and SST<sup>+</sup> IN density was not altered in MC in adults (PV: WT  $2.72 \pm 0.30$  cells/10,000  $\mu\text{m}^2$ , cKO  $2.36 \pm 0.47$  cells/10,000  $\mu\text{m}^2$ ; SST: WT  $2.24 \pm 0.66$  cells/10,000  $\mu\text{m}^2$ , cKO  $2.60 \pm 0.92$  cells/10,000  $\mu\text{m}^2$ , Fig. 3B,C), similar to the SSC, but both were reduced in adult PFC (PV: WT  $2.78 \pm 0.48$  cells/10,000  $\mu\text{m}^2$ , cKO  $1.23 \pm 0.24$  cells/10,000  $\mu\text{m}^2$ ; SST: WT  $2.28 \pm 0.36$  cells/10,000  $\mu\text{m}^2$ , cKO  $1.21 \pm 0.17$  cells/10,000  $\mu\text{m}^2$ , Fig. 3E,F), consistent with a previous study (Pirone et al., 2018).

#### Immature PV<sup>+</sup> in cell density is altered in APC cKO mice using Lhx6-GFP mice

To confirm that immature PV<sup>+</sup> IN density is lower in APC cKO mice at P9, we repeated this experiment using Lhx6-GFP mice, a different genetic reporter line in which all MGE-derived INs (PV<sup>+</sup> and SST<sup>+</sup>) are labeled with GFP. Because SST protein is robustly expressed early in cortical development, immature PV<sup>+</sup> INs can be identified as cells that are Lhx6-GFP<sup>+</sup> but SST immunonegative (Liadis et al., 2007; Alroy et al., 2008). The density of all Lhx6-GFP<sup>+</sup> INs (representing both PV<sup>+</sup> and SST<sup>+</sup> INs) was significantly decreased in the SSC for APC cKO mice at P9 (cKO density  $3.47 \pm 0.47$  cells/10,000  $\mu\text{m}^2$ ; WT density  $5.33 \pm 0.37$  cells/10,000  $\mu\text{m}^2$ ; Fig. 4A,B). Next, we quantified the density of Lhx6 INs that are SST<sup>+</sup> (Lhx6<sup>+</sup>/SST<sup>+</sup>) at P9 and found there was no difference between WT and cKO (cKO density  $0.56 \pm 0.10$  cells/10,000  $\mu\text{m}^2$ ; WT density  $0.68 \pm 0.09$  cells/10,000  $\mu\text{m}^2$ ; Fig. 4A,C). The density of immature PV<sup>+</sup> INs (Lhx6-GFP<sup>+</sup>/SST<sup>-</sup>) was calculated by subtracting the Lhx6-GFP<sup>+</sup>/SST<sup>+</sup> cell density from total Lhx6-GFP<sup>+</sup> cell density. Using this approach, we found that immature PV<sup>+</sup> IN density was again decreased in APC cKO mice at P9 (cKO density  $2.92 \pm 0.40$  cells/10,000  $\mu\text{m}^2$ ; WT density  $4.64 \pm 0.43$  cells/10,000

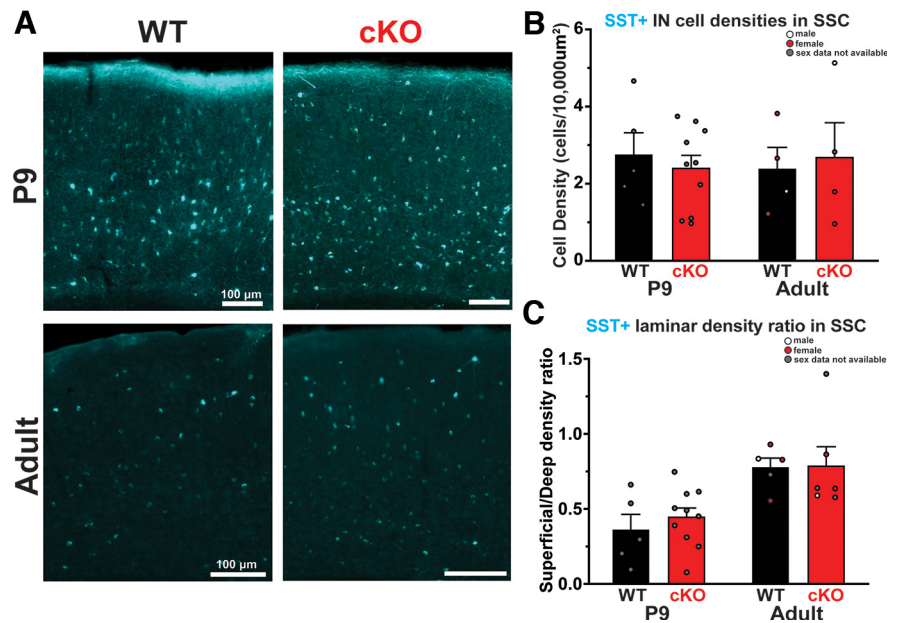


**Figure 2.** SST<sup>+</sup> IN density does not differ in the SSC of APC cKO mice. **A**, Representative fluorescent images in SSC of SST<sup>+</sup> immunolabeled (cyan) cells at (top) P9 and (bottom) adult in WT and cKO mice. Scale bar, 100  $\mu\text{m}$ . **B**, Bar graph of average SST<sup>+</sup> IN cell density per animal at P9 for WT (black bar,  $n = 5$  animals) and cKO (red bar,  $n = 10$  animals) mice ( $p = 0.58$ ,  $t_{(13)} = 0.57$ , two-sample  $t$  test;  $p = 0.56$ ,  $t_{(36)} = 0.60$ , LMM) and adult WT ( $n = 4$  animals) and cKO ( $n = 4$  animals;  $p = 0.79$ ,  $t_{(6)} = 0.28$ , two-sample  $t$  test;  $p = 0.74$ ,  $t_{(8)} = -0.34$ , LMM). **C**, Bar graph of the laminar density ratio, which represents the ratio of superficial layer densities to deep layer densities, of SST<sup>+</sup> INs at P9 in WT (black bar,  $n = 5$  animals) and cKO (red bar,  $n = 10$  animals) mice ( $p = 0.47$ ,  $t_{(13)} = -0.74$ , two-sample  $t$  test;  $p = 0.41$ ,  $t_{(39)} = -0.84$ , LMM) and adult WT ( $n = 5$  animals) and cKO ( $n = 6$  animals;  $p = 0.95$ ,  $t_{(9)} = -0.06$ , two-sample  $t$  test;  $p = 0.94$ ,  $t_{(20)} = -0.08$ , LMM). \* $p < 0.05$ , two-sample  $t$  test. # $p < 0.05$ , LMM, effect of genotype. Each data point represents the average ratio for 1 animal. Symbol interior color represents sex data. Error bars indicate SEM.

$\mu\text{m}^2$ ; Fig. 4A,D). In adult APC cKO mice, we found that there was no difference in either Lhx6-GFP<sup>+</sup> (cKO density  $2.51 \pm 0.27$  cells/10,000  $\mu\text{m}^2$ ; WT density  $3.46 \pm 0.41$  cells/10,000  $\mu\text{m}^2$ ; Fig. 4E,F) or in double-positive PV<sup>+</sup>/Lhx6-GFP<sup>+</sup> cells (cKO density  $1.06 \pm 0.15$  cells/10,000  $\mu\text{m}^2$ ; WT density  $1.52 \pm 0.19$  cells/10,000  $\mu\text{m}^2$ ; Fig. 4E,G; this results in labeling of a subset of PV<sup>+</sup> INs that are GFP<sup>+</sup> in the Lhx6-GFP line). Together, these studies show that immature PV<sup>+</sup> INs are decreased in the P9 SSC in APC cKO mice. For the subsequent experiments, G42 reporter mice were used to identify immature PV<sup>+</sup> INs.

#### Immature G42-GFP<sup>+</sup> PV<sup>+</sup> INs undergo disproportionate developmental apoptosis in APC cKO mice

Cortical INs are produced in excess during embryonic development (Denaxa et al., 2018), and their final numbers are established through a process of intrinsic apoptosis wherein death occurs  $\sim 12$  d after genesis, unless prevented by external neuronal activity (Southwell et al., 2012; Wong et al., 2018). Although the threshold of excitatory input necessary to confer survival is not established, IN survival is improved by calcium influx and action potential generation (Priya et al., 2018). MGE-derived IN cell death peaks at approximately P7–P9, the time of peak behavioral spasms in APC cKO mice. We hypothesized that decreased PV<sup>+</sup> IN density in neonatal APC cKO cortex may arise from altered developmental apoptosis.

To investigate the developmental apoptosis of PV<sup>+</sup> INs during early development, we used an antibody against cleaved caspase 3 (Cl-CASP3<sup>+</sup>), a marker of apoptosis. We examined three developmental time windows: P3–P5 (before behavioral spasm onset), P7–P9 (during the peak of behavioral spasms), and P14

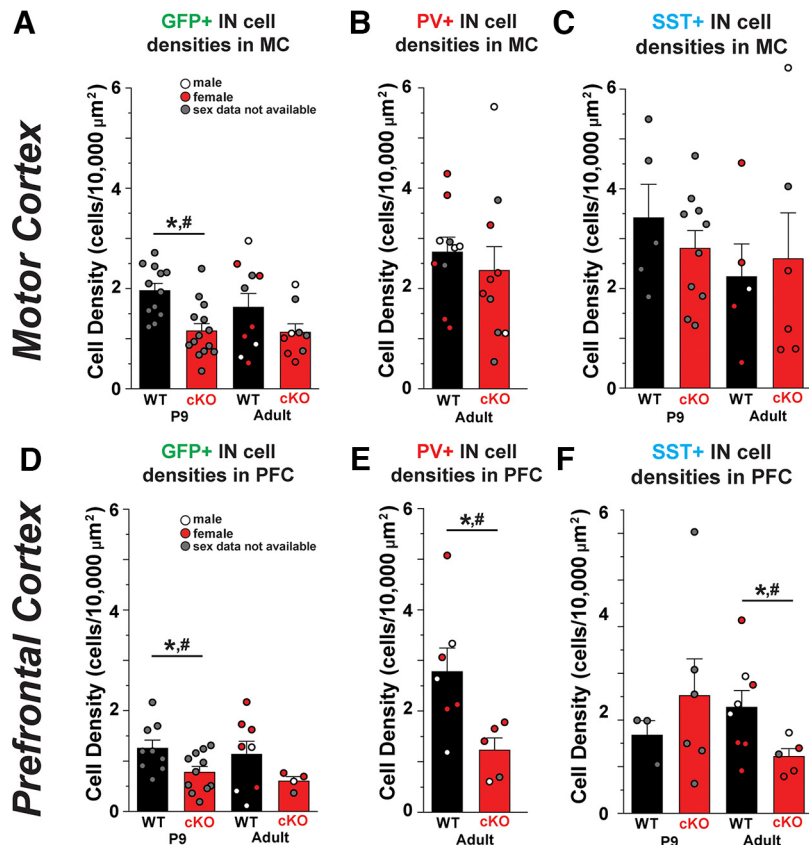


**Figure 3.** Changes in G42-GFP<sup>+</sup>, PV<sup>+</sup>, and SST<sup>+</sup> INs in the motor and PFC. **A**, Bar graph of the average G42-GFP<sup>+</sup> IN density in the motor cortex in P9 WT ( $n = 12$  animals) and cKO ( $n = 14$  animals;  $p = 6.92e-4$ ,  $t_{(24)} = 3.89$ , two-sample  $t$  test;  $p = 6.24e-4$ ,  $t_{(73)} = 3.86$ , LMM); and adult WT ( $n = 10$  animals) and cKO ( $n = 9$  animals;  $p = 0.15$ ,  $t_{(17)} = 1.52$ , two-sample  $t$  test;  $p = 0.14$ ,  $t_{(40)} = 1.55$ , LMM). **B**, PV<sup>+</sup> immunolabeled IN densities in the motor cortex of adult WT ( $n = 10$  animals) and cKO ( $n = 10$  animals;  $p = 0.53$ ,  $t_{(18)} = 0.65$ , two-sample  $t$  test;  $p = 0.76$ ,  $t_{(36)} = -0.32$ , LMM) mice. **C**, Bar graph of the average SST<sup>+</sup> IN density in the motor cortex of P9 WT ( $n = 5$  animals) and cKO ( $n = 10$  animals;  $p = 0.39$ ,  $t_{(13)} = 0.89$ , two-sample  $t$  test;  $p = 0.40$ ,  $t_{(60)} = 0.86$ , LMM); and adult WT ( $n = 5$  animals) and cKO ( $n = 6$  animals;  $p = 0.77$ ,  $t_{(9)} = 0.30$ , two-sample  $t$  test;  $p = 0.69$ ,  $t_{(22)} = -0.41$ , LMM) mice. **D**, Bar graph of the average G42-GFP<sup>+</sup> IN density in the PFC of P9 WT ( $n = 9$  animals) and cKO ( $n = 11$  animals;  $p = 0.02$ ,  $t_{(18)} = 2.45$ , two-sample  $t$  test;  $p = 0.02$ ,  $t_{(21)} = 2.66$ , LMM); and adult WT ( $n = 8$  animals) and cKO ( $n = 4$  animals;  $p = 0.19$ ,  $t_{(10)} = 1.40$ , two-sample  $t$  test;  $p = 0.15$ ,  $t_{(18)} = 1.52$ , LMM) mice. **E**, PV<sup>+</sup> immunolabeled IN densities in the PFC of adult WT ( $n = 7$  animals) and cKO ( $n = 5$  animals;  $p = 0.03$ ,  $t_{(10)} = 2.60$ , two-sample  $t$  test;  $p = 0.01$ ,  $t_{(13)} = 3.02$ , LMM) mice. **F**, Bar graph of the average SST<sup>+</sup> IN densities in the PFC of P9 WT ( $n = 3$  animals) and cKO ( $n = 6$  animals;  $p = 0.49$ ,  $t_{(7)} = 0.72$ , two-sample  $t$  test;  $p = 0.47$ ,  $t_{(10)} = -0.76$ , LMM); and adult WT ( $n = 8$  animals) and cKO ( $n = 5$  animals;  $p = 4.95e-2$ ,  $t_{(11)} = 2.21$ , two-sample  $t$  test;  $p = 0.03$ ,  $t_{(25)} = 2.33$ , LMM) mice. \* $p < 0.05$ , two-sample  $t$  test. # $p < 0.05$ , LMM, effect of genotype. Each data point represents the average ratio for 1 animal. Symbol interior color represents sex data. Error bars indicate SEM.

(after spasms stop) (Pirone et al., 2017). G42-GFP<sup>+</sup> IN density was decreased in P7–P9 APC cKO mice (cKO density  $1.51 \pm 0.28$  cells/10,000  $\mu\text{m}^2$ ; WT density  $2.30 \pm 0.23$  cells/10,000  $\mu\text{m}^2$ ; Fig. 5B), consistent with data in Figure 1. The density of G42-GFP<sup>+</sup> INs that colabeled for Cl-CASP3<sup>+</sup> (G42-GFP<sup>+</sup>/Cl-CASP3<sup>+</sup>) was unchanged from P3–5 and P7–9, but was significantly decreased at P14 (cKO density  $0.44 \pm 0.09$  cells/10,000  $\mu\text{m}^2$ ; WT density  $1.05 \pm 0.26$  cells/10,000  $\mu\text{m}^2$ ; Fig. 5C). Because the number of G42-GFP<sup>+</sup> INs was not equivalent in WT and APC cKO mice, we next asked whether the proportion of G42-GFP<sup>+</sup> cells undergoing apoptosis was altered in APC cKOs. At P3–P5, the percentage of G42-GFP<sup>+</sup> cells that were colabeled by Cl-CASP3<sup>+</sup> was similar in APC cKO and WT mice (cKO ratio  $0.31 \pm 0.05$ ; WT ratio  $0.27 \pm 0.04$ ; Fig. 5D). However, from P7–P9, there were significantly more G42-GFP<sup>+</sup> INs that were Cl-CASP3<sup>+</sup> in APC cKO mice compared with WT (cKO ratio  $0.71 \pm 0.05$ ; WT ratio  $0.50 \pm 0.05$ ; Fig. 5A,D). This increase is likely driven by the fact that there are less G42-GFP<sup>+</sup>

INs in the SSC at this time point (Fig. 5B,C). At P14, APC cKO mice had significantly fewer G42-GFP<sup>+</sup> cells that were Cl-CASP3<sup>+</sup> (cKO ratio  $0.28 \pm 0.05$ ; WT ratio  $0.55 \pm 0.08$ ; Fig. 4D), suggesting that developmental cell death in PV<sup>+</sup> INs ends earlier in the cKO. Because developmental apoptosis of PV<sup>+</sup> INs is activity-dependent, we next asked whether excitation of PV<sup>+</sup> INs was disrupted in early development in APC cKO mice.

### Synaptic excitation of PV<sup>+</sup> INs is increased in APC cKO mice

Whole-cell voltage-clamp recordings were made from layer 5 G42-GFP<sup>+</sup> INs in APC WT and cKO mice at P9, P14, the ages of altered developmental apoptosis, and in adults (>P60). sEPSCs were recorded, and frequency and amplitude were quantified. At all ages, the mean frequency of sEPSCs onto PV<sup>+</sup> INs was increased in APC cKOs compared with WT mice (P9 cKO  $2.70 \pm 0.55$  Hz; P9 WT  $0.97 \pm 0.12$  Hz; P14 cKO  $8.73 \pm 1.31$  Hz; P14 WT  $4.96 \pm 0.98$  Hz; P60 cKO  $6.46 \pm 1.87$  Hz; P60 WT  $2.65 \pm 0.41$ ; Fig. 6). In addition, the cumulative distribution of sEPSC IEs was significantly shifted to the left, consistent with more frequent synaptic excitation (Fig. 6D–F). Mean sEPSC amplitude was similar in APC cKOs and WT mice at all ages (P9 cKO  $18.5 \pm 1.59$  pA; P9 WT  $22.8 \pm 2.88$  pA; P14 cKO  $16.1 \pm 1.94$  pA; P14 WT  $19.7 \pm 2.47$  pA; P60 cKO  $23.8 \pm 4.49$  pA; P60 WT  $20.6 \pm 2.80$  pA; Fig. 6), but the cumulative distribution of sEPSC amplitudes was left-shifted at P9 and P14, suggesting smaller sEPSCs in APC cKO mice (Fig. 6D,E).

We next quantified action potential-independent mEPSCs in layer 5 G42-GFP<sup>+</sup> INs. At P9, the mean frequency of mEPSCs (cKO  $2.60 \pm 0.44$  Hz; WT  $0.89 \pm 0.20$  Hz; Fig. 7A,D) was significantly increased and the cumulative distribution of mEPSC IEs was significantly left-shifted in APC cKO mice (Fig. 7D). At P14 and P60, however, mEPSC frequency was equivalent in APC cKO and WT mice (P14 cKO  $5.74 \pm 1.19$  Hz; P14 WT  $5.73 \pm 1.01$  Hz; Fig. 7B,E; P60 cKO  $4.46 \pm 1.14$  Hz; P60 WT  $3.73 \pm 0.61$  Hz; Fig. 7C,F). mEPSC amplitude was equivalent in APC cKOs and WT mice at all ages as well (P9 cKO  $16.3 \pm 1.36$  pA; P9 WT  $15.7 \pm 1.30$  pA; P14 cKO  $16.1 \pm 1.13$  pA; P14 WT  $16.3 \pm 1.20$  pA; P60 cKO  $12.2 \pm 1.44$  pA; P60 WT  $12.8 \pm 1.06$  pA; Fig. 7). In conclusion, G42-GFP<sup>+</sup> INs in APC cKOs receive an increased frequency of sEPSCs at all ages examined, but mEPSC frequency onto INs was increased only at P9. This is consistent with known increases in synaptic excitation in APC cKOs (Pirone et al., 2017).

### Dendrite morphology is altered in immature PV<sup>+</sup> INs in APC cKO mice

Cortical excitation guides PV<sup>+</sup> IN morphologic maturation, including dendritogenesis (Murase et al., 2002; Konur and Ghosh, 2005;

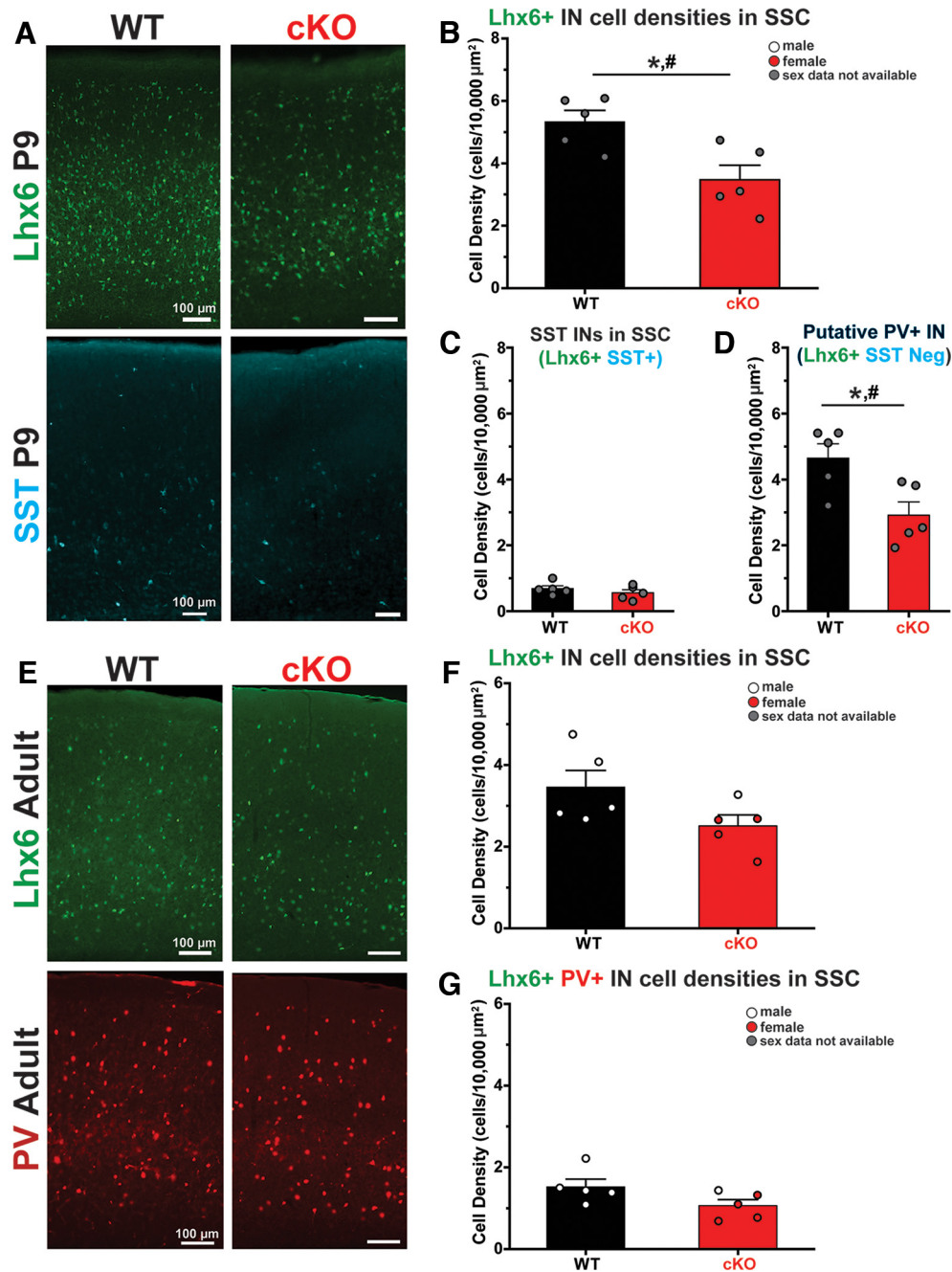


**Figure 4.** Immature PV<sup>+</sup> IN density, as measured using Lhx6-GFP mice, is reduced in the SSC of APC cKO mice at P9. **A**, Representative fluorescent images in SSC of Lhx6<sup>+</sup> cells (top, green, labeling MGE-derived INs) and SST<sup>+</sup> cells (bottom, cyan) at P9 in WT and cKO mice. Scale bar, 100 μm. **B**, Bar graph of average Lhx6<sup>+</sup> IN (all MGE-derived INs) density per animal from SSC at P9 in WT (black,  $n = 5$  animals) and cKO (red,  $n = 5$  animals;  $p = 0.01$ ,  $t_{(8)} = 3.12$ , two-sample  $t$  test;  $p = 6.59 \times 10^{-3}$ ,  $t_{(15)} = 3.41$ , LMM) mice. **C**, Bar graph of average Lhx6<sup>+</sup>/SST<sup>+</sup> IN (genetically Lhx6<sup>+</sup> and SST immune-positive) density per animal at P9 in WT ( $n = 5$  animals) and cKO ( $n = 5$  animals;  $p = 0.35$ ,  $t_{(8)} = 0.99$ , two-sample  $t$  test;  $p = 0.29$ ,  $t_{(15)} = 1.10$ , LMM) mice. **D**, Bar graph of average putative PV<sup>+</sup> IN (genetically Lhx6<sup>+</sup> and SST immune-negative) density per animal at P9 in WT ( $n = 5$  animals) and cKO ( $n = 5$  animals;  $p = 0.02$ ,  $t_{(8)} = 2.92$ , two-sample  $t$  test;  $p = 0.01$ ,  $t_{(15)} = 3.19$ , LMM) mice. **E**, Representative fluorescent images in SSC of Lhx6<sup>+</sup> cells (top) and PV<sup>+</sup> immunolabeled cells (red, bottom) in adult WT and cKO mice. **F**, Bar graph of average Lhx6<sup>+</sup> IN density per animal from SSC in adult WT ( $n = 5$  animals) and cKO ( $n = 5$  animals;  $p = 0.09$ ,  $t_{(8)} = -1.94$ , two-sample  $t$  test;  $p = 0.06$ ,  $t_{(14)} = 2.12$ , LMM) mice. **G**, Bar graph of average Lhx6<sup>+</sup>/PV<sup>+</sup> IN density per animal from immunolabeling in adult WT ( $n = 5$  animals) and cKO ( $n = 5$  animals;  $p = 0.09$ ,  $t_{(8)} = -1.92$ , two-sample  $t$  test;  $p = 0.06$ ,  $t_{(14)} = 2.10$ , LMM) mice. \* $p < 0.05$ , two-sample  $t$  test. # $p < 0.05$ , LMM, effect of genotype. Each data point represents the average density for 1 animal. Symbol interior color represents sex data. Error bars indicate SEM.

Close et al., 2012; Wamsley and Fishell, 2017). Since PV<sup>+</sup> INs receive increased excitation in APC cKO mice, we suspected that their dendritic morphology may also be altered. To address this question, layer 5 G42-GFP<sup>+</sup> INs were biocytin-filled, their dendrites were morphologically reconstructed, and the number of dendritic intersections at increasing radii from the soma was quantified using Scholl analysis. To analyze P9 dendritic morphology

with LMM, we fit a piecewise linear mixed effects model, including a knot, or change in slope, at a radius of 60 μm (Fig. 8A,B) for data collected from 0 to 300 μm from the soma. The piecewise linear mixed effects model showed that, for radii <60 μm, the number of intersections increase more quickly for cKO mice than for WT mice at P9 (cKO slope = 0.28 μm/intersections, WT slope = 0.20 μm/intersections) and no difference from 60 to 300 μm at P9 (cKO

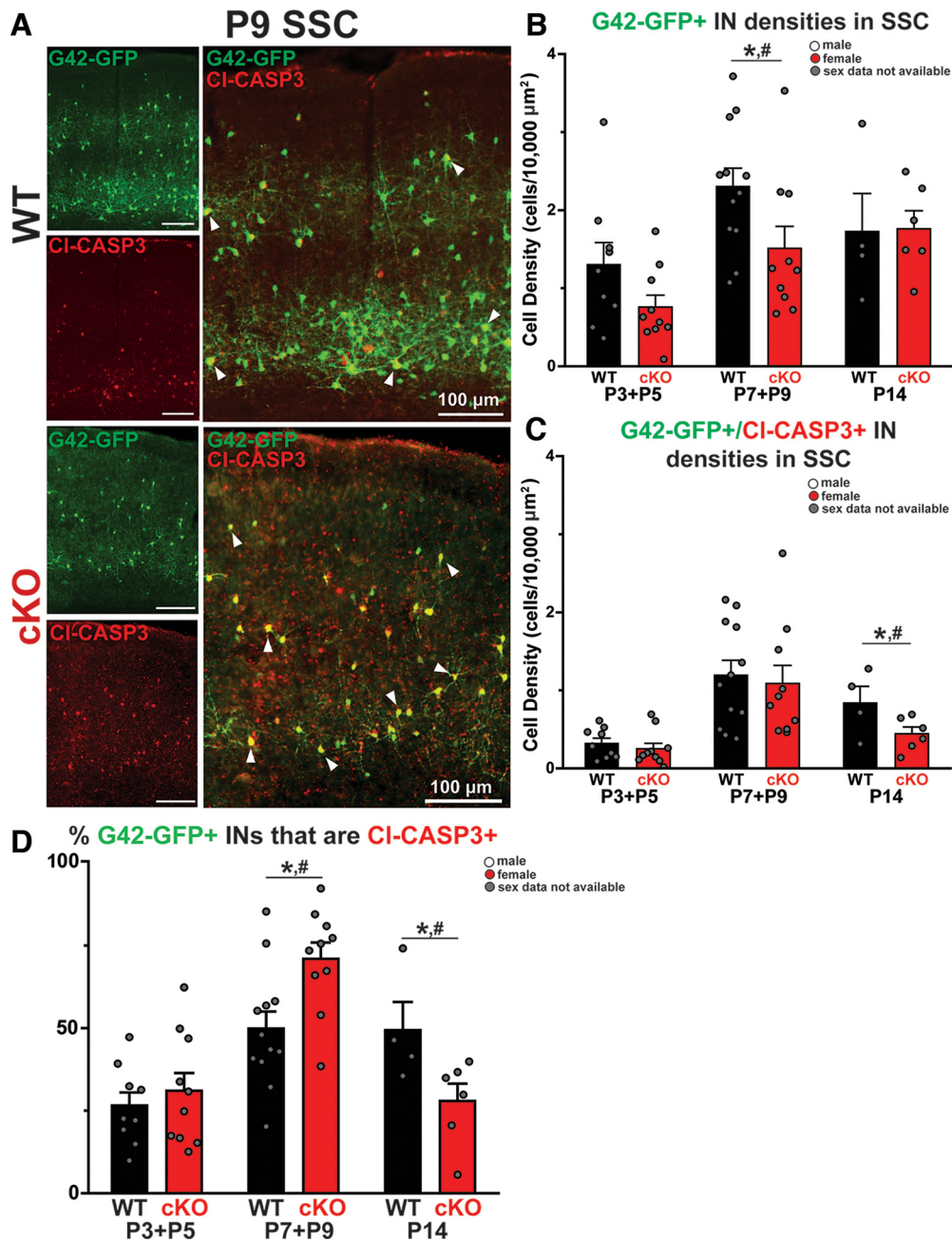


**Figure 5.** APC cKO mice show disrupted developmental IN apoptosis in G42-labeled cells. **A**, Representative fluorescent images in SSC of G42-GFP<sup>+</sup> (green) cells, CI-Caspase3 (CI-CASP<sup>+</sup>, red) immunolabeled cells, and overlays from P9 (top) WT and (bottom) cKO mice. Scale bar, 100  $\mu$ m. Yellow cells represent a G42-GFP<sup>+</sup> IN colabeled with CI-CASP antibody (right). White arrows indicate representative colabeled cells. **B**, Bar graph of the average G42-GFP<sup>+</sup> IN density in P3–P5 WT ( $n = 9$  animals) and cKO ( $n = 10$  animals;  $p = 0.10$ ,  $t_{(17)} = -1.75$ , two-sample  $t$  test;  $p = 0.07$ ,  $t_{(65)} = 1.94$ , LMM), P7–P9 WT ( $n = 12$  animals) and cKO ( $n = 10$  animals;  $p = 0.04$ ,  $t_{(20)} = 2.19$ , two-sample  $t$  test;  $p = 0.04$ ,  $t_{(40)} = 2.18$ , LMM), and P14 WT ( $n = 5$  animals) and cKO ( $n = 6$  animals;  $p = 0.79$ ,  $t_{(9)} = -0.27$ , two-sample  $t$  test;  $p = 0.77$ ,  $t_{(15)} = 0.30$ , LMM) mice. **C**, Bar graph of the average G42-GFP<sup>+</sup>, CI-CASP3<sup>+</sup> IN density in P3–P5 WT ( $n = 9$  animals) and cKO ( $n = 10$  animals;  $p = 0.47$ ,  $t_{(17)} = -0.74$ , two-sample  $t$  test;  $p = 0.10$ ,  $t_{(65)} = 1.74$ , LMM), P7–P9 WT ( $n = 12$  animals) and cKO ( $n = 10$  animals;  $p = 0.72$ ,  $t_{(20)} = 0.37$ , two-sample  $t$  test;  $p = 0.85$ ,  $t_{(40)} = 0.20$ , LMM), and P14 WT ( $n = 5$  animals) and cKO ( $n = 6$  animals;  $p = 0.04$ ,  $t_{(9)} = -2.35$ , two-sample  $t$  test;  $p = 0.02$ ,  $t_{(15)} = 2.59$ , LMM) mice. **D**, Bar graph of the average percentage G42-GFP<sup>+</sup> cells that are CI-CASP<sup>+</sup> in P3–P5 WT (black bar,  $n = 9$  animals) and cKO (red bar,  $n = 10$  animals;  $p = 0.52$ ,  $t_{(17)} = 0.66$ , two-sample  $t$  test;  $p = 0.94$ ,  $t_{(59)} = -0.08$ , LMM), P7–P9 WT ( $n = 12$  animals) and cKO ( $n = 10$  animals;  $p = 8.62 \times 10^{-3}$ ,  $t_{(20)} = -2.91$ , two-sample  $t$  test;  $p = 2.53 \times 10^{-3}$ ,  $t_{(40)} = -3.43$ , LMM), and P14 WT ( $n = 5$  animals) and cKO ( $n = 6$  animals;  $p = 0.02$ ,  $t_{(9)} = -2.79$ , two-sample  $t$  test;  $p = 0.01$ ,  $t_{(16)} = 3.16$ , LMM). \* $p < 0.05$ , two-sample  $t$  test. # $p < 0.05$ , LMM, effect of genotype. Each data point represents the average density or ratio for 1 animal. Symbol interior color represents sex data. Error bars indicate SEM.

slope =  $-0.13 \mu\text{m}/\text{intersections}$ , WT slope =  $-0.10 \mu\text{m}/\text{intersections}$ ). G42<sup>+</sup> INs morphology was similar in WT and APC cKO when examined at P14 (Fig. 8C,D) and P60 (Fig. 8E,F). The increase in dendritic complexity at P9 is consistent with increased mEPSC frequency (Fig. 7A,D), as more dendritic processes may be able to receive more excitatory synaptic input.

#### Dynamic developmental changes in GABAergic synaptic transmission in APC cKO mice

Because the excitation of PV<sup>+</sup> INs is enhanced in APC cKOs, we suspected that GABAergic output may also be altered. We therefore made whole-cell recordings from layer 5 excitatory pyramidal neurons (L5Ps) in the SSC at P9, P14, and P60 in APC cKO and WT mice and quantified GABAergic synaptic transmission.

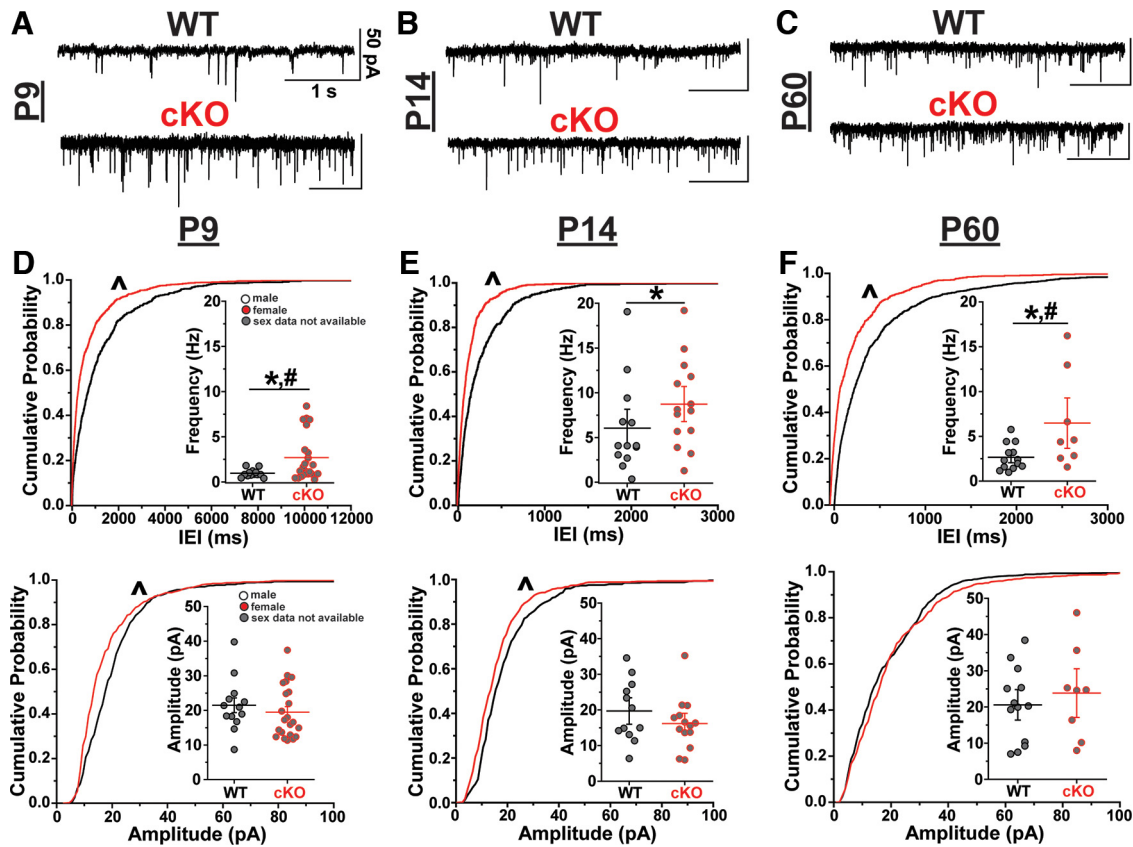


**Figure 6.** Increased sEPSCs onto G42-GFP<sup>+</sup> INs in the cortex of the APC cKO. Example sEPSC traces from voltage-clamped, L5 G42-GFP<sup>+</sup> INs held at  $-60$  mV at (A) P9, (B) P14, and (C) P60 for WT (black) and cKO (red) mice. All recordings made in SSC. Calibration: 50 pA, 1 s. **D**, Cumulative probability plots of IELs ( $p = 5.23e-19$ , K-S test) with inset of mean frequency for WT (black,  $n = 13$  cells, 4 animals) and cKO (red,  $n = 22$  cells, 6 animals;  $p = 0.03$ ,  $t_{(32)} = -2.32$ , two-sample  $t$  test;  $p = 0.04$ ,  $t_{(28)} = -2.19$ , LMM) and amplitude ( $p = 5.36e-14$ , K-S test) with inset of mean amplitude for WT ( $n = 13$  cells, 4 animals) and cKO ( $n = 18$  cells, 6 animals;  $p = 0.17$ ,  $t_{(29)} = 1.40$ , two-sample  $t$  test;  $p = 0.23$ ,  $t_{(30)} = 1.22$ , LMM) at P9. **E**, Cumulative probability plots of IELs ( $p = 1.85e-12$ , K-S test) with inset of mean frequency for WT ( $n = 14$  cells, 6 animals) and cKO ( $n = 12$  cells, 5 animals;  $p = 0.03$ ,  $t_{(24)} = -2.25$ ;  $p = 0.49$ ,  $t_{(22)} = -0.73$ , LMM) and amplitude ( $p = 1.63e-5$ ; K-S test) with inset of mean amplitude for WT ( $n = 12$  cells, 6 animals) and cKO ( $n = 14$  cells, 5 animals;  $p = 0.27$ ,  $t_{(24)} = 1.14$ , two-sample  $t$  test;  $p = 0.40$ ,  $t_{(22)} = 0.88$ , LMM) at P14. **F**, Cumulative probability plots of IELs ( $p = 6.93e-13$ , K-S test) with inset of mean frequency for WT ( $n = 13$  cells, 5 animals) and cKO ( $n = 8$  cells, 4 animals;  $p = 0.02$ ,  $t_{(19)} = -2.48$ , two-sample  $t$  test;  $p = 0.02$ ,  $t_{(16)} = -2.57$ , LMM) and amplitude ( $p = 0.02$ , K-S test) with inset of mean amplitude for WT ( $n = 13$  cells, 5 animals) and cKO ( $n = 8$  cells, 4 animals;  $p = 0.52$ ,  $t_{(19)} = -0.65$ , two-sample  $t$  test;  $p = 0.95$ ,  $t_{(16)} = 0.06$ , LMM) at P60.  $\wedge p < 0.00001$ , KS test.  $*p < 0.05$ , two-sample  $t$  test.  $\#p < 0.05$ , LMM, effect of genotype. Each data point represents one cell. Symbol interior color represents sex data. Data for inset graphs are mean  $\pm$  SEM.

Consistent with published reports (Luhmann and Prince, 1991; Le Magueresse and Monyer, 2013), the frequency of IPSCs was very low at young ages and increased over time in both APC cKOs and WT mice. Interestingly, changes in GABAergic synaptic transmission were complex in APC cKOs with developmentally specific changes in IPSC frequency and amplitude. At P9, the cumulative distribution of sIPSC amplitude was significantly right-shifted in APC cKOs, consistent with larger sIPSCs (Fig. 9A,D), but the frequency of sIPSCs was normal (cKO  $2.03 \pm 0.75$  Hz; WT  $1.20 \pm 0.36$ ; Fig. 9A,D). At P14, the mean sIPSC frequency was significantly decreased (cKO  $5.77 \pm 0.77$  Hz; WT  $8.86 \pm 1.26$  Hz; Fig. 9B,E) and the cumulative distribution of sIPSC IEI was significantly right-shifted in APC cKO mice (Fig. 9E), consistent with less frequent sIPSCs. At P14, the amplitude of sIPSCs was normal (cKO  $18.6 \pm 2.04$  pA; WT  $20.3 \pm 1.46$  pA; Fig. 9B,E). At P60, the mean sIPSC amplitude was significantly larger (cKO  $21.3 \pm 1.60$  pA; WT  $13.0 \pm 0.74$  pA; Fig. 9C,F) and cumulative distribution was significantly right-shifted, consistent with larger sIPSCs while the frequency of sIPSCs was unaltered (Fig. 9F).

When quantifying mIPSCs, we found that mean mIPSC frequency was not changed at any age (Fig. 10), but the cumulative distribution of mIPSC IEI was left-shifted in P9 APC cKOs,

compared with WT, which appears to be driven by the distribution of cKO mice having less non-zero values (Fig. 10A,D). At P14, there was no difference in mIPSC frequency (cKO  $4.31 \pm 1.01$  Hz; WT  $4.00 \pm 0.85$  Hz; Fig. 10B,E) or amplitude (cKO  $16.3 \pm 0.94$  pA; WT  $17.3 \pm 1.18$  pA; Fig. 10B,E) between APC cKO and WT mice. At P60, the mean mIPSC amplitude was significantly increased (cKO  $21.6 \pm 2.10$  pA; WT  $12.7 \pm 0.98$  pA; Fig. 10C,F) and the cumulative distribution of mIPSC amplitude was right-shifted (Fig. 10F), consistent with larger mIPSCs. Interestingly, mIPSC amplitude in APC cKO mice was significantly affected by sex at P60. Female APC cKO mice had significantly larger mIPSCs ( $24.9 \pm 2.16$  pA,  $n = 5$  cells, 2 animals) compared with APC cKO males ( $16.2 \pm 1.46$  pA,  $n = 3$  cells, 2 animals; Fig. 10F) at this age.

In conclusion, L5Ps receive disrupted GABAergic input at all ages we examined. Most significantly, GABAergic synaptic transmission is increased onto L5Ps at P9, decreased at P14, and again increased at P60. We suspect that this is driven by premature increases in synaptic excitation of PV<sup>+</sup> INs at P9, leading to increased GABAergic output, followed by compensatory changes that result in decreased sIPSC frequency at P14. In P60 animals, increased sIPSC/mIPSC amplitude suggests further compensation, perhaps in response to abnormal synaptic excitation and seizures known to exist in APC cKOs.

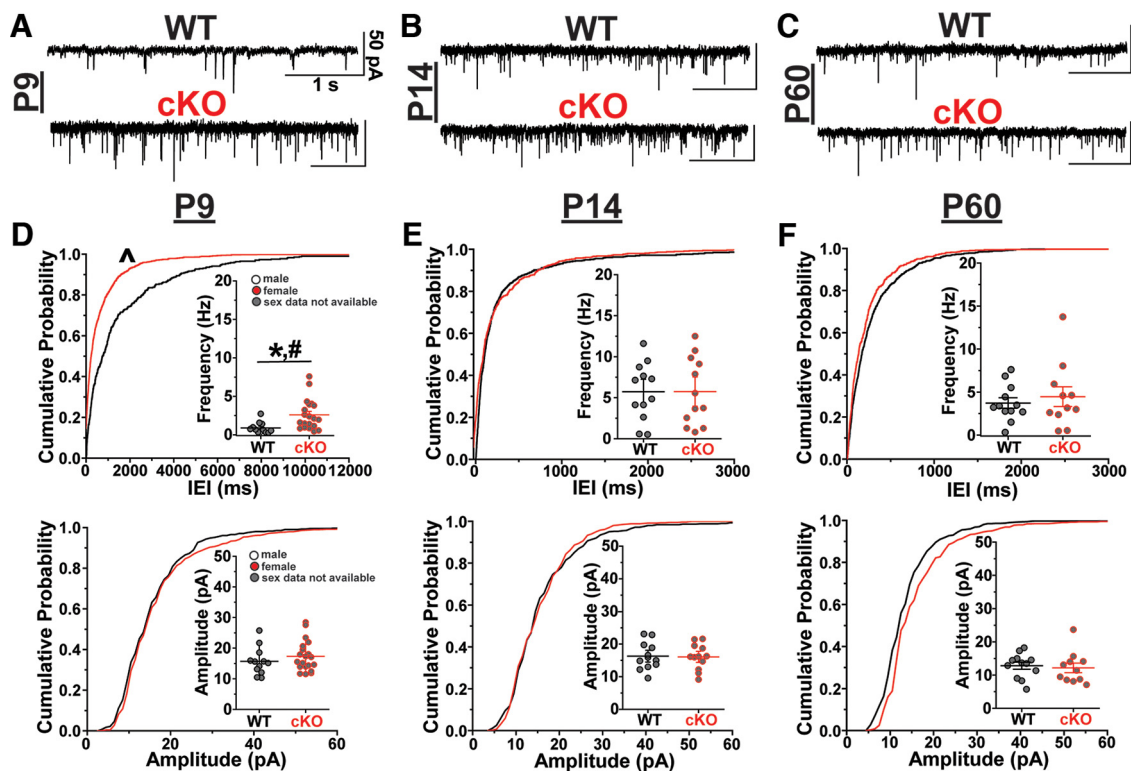


**Figure 7.** Increased mEPSCs onto G42-GFP<sup>+</sup> INs at P9 in the APC cKO. Example mEPSC traces from voltage-clamped, L5 G42-GFP<sup>+</sup> INs held at  $-60$  mV at (A) P9, (B) P14, and (C) P60 for WT (black) and cKO (red) mice. All recordings made in SSC. Calibration: 50 pA, 1 s. D, Cumulative probability plots of IELs ( $p = 9.67 \times 10^{-16}$ , K-S test) with inset of mean frequency for WT (black,  $n = 12$  cells, 3 animals) and cKO (red,  $n = 20$  cells, 5 animals;  $p = 0.01$ ,  $t_{(24)} = -2.77$ , two-sample  $t$  test;  $p = 0.02$ ,  $t_{(27)} = -2.71$ , LMM) and amplitude ( $p = 0.03$ , K-S test) with inset of mean amplitude for WT ( $n = 12$  cells, 3 animals) and cKO ( $n = 13$  cells, 5 animals;  $p = 0.75$ ,  $t_{(23)} = -0.33$ , two-sample  $t$  test;  $p = 0.10$ ,  $t_{(27)} = -1.70$ , LMM) at P9. E, Cumulative probability plots of IELs ( $p = 0.10$ , K-S test) with inset of mean frequency for WT ( $n = 12$  cells, 6 animals) and cKO ( $n = 12$  cells, 6 animals;  $p = 0.99$ ,  $t_{(22)} = -0.01$ , two-sample  $t$  test;  $p = 0.54$ ,  $t_{(21)} = 0.64$ , LMM) and amplitude ( $p = 0.76$ , K-S test) with inset of mean amplitude for WT ( $n = 12$  cells, 6 animals) and cKO ( $n = 12$  cells, 6 animals;  $p = 0.90$ ,  $t_{(22)} = 0.13$ , two-sample  $t$  test;  $p = 0.77$ ,  $t_{(21)} = 0.30$ , LMM) at P14. F, Cumulative probability plots of IELs ( $p = 1.20 \times 10^{-3}$ , K-S test) with inset of mean frequency for WT ( $n = 12$  cells, 4 animals) and cKO ( $n = 11$  cells, 3 animals;  $p = 0.57$ ,  $t_{(21)} = -0.58$ , two-sample  $t$  test;  $p = 0.52$ ,  $t_{(17)} = -0.67$ , LMM) and amplitude ( $p = 2.20 \times 10^{-3}$ , K-S test) with inset of mean amplitude for WT ( $n = 12$  cells, 4 animals) and cKO ( $n = 11$  cells, 3 animals;  $p = 0.71$ ,  $t_{(21)} = 0.37$ , two-sample  $t$  test;  $p = 0.88$ ,  $t_{(17)} = 0.16$ , LMM) at P60.  $\wedge p < 0.00001$ , KS test. \* $p < 0.05$ , two-sample  $t$  test. # $p < 0.05$ , LMM, effect of genotype. Each data point represents one cell. Symbol interior color represents sex data. Data for inset graphs are mean  $\pm$  SEM.

### Intrinsic excitability of PV<sup>+</sup> INs is reduced in APC cKO mice

Finally, to ascertain whether altered PV<sup>+</sup> IN maturation in APC cKO mice changed the intrinsic electrophysiological and action potential firing properties of these cells, we performed current-clamp recordings from G42-GFP<sup>+</sup> INs in layer 5 SSC at P9, P14, and P60 (Fig. 11). Consistent with published findings, these properties changed over time, reflecting the normal development of PV<sup>+</sup> INs (Pangratz-Fuehrer and Hestrin, 2011). Resting membrane potential, membrane resistance, rheobase, and capacitance were similar in WT and cKO mice at all ages examined (Fig. 11C–E). Interestingly, PV<sup>+</sup> INs fired fewer action potentials in response to depolarizing current injections at all ages in APC cKO mice compared with WT (Fig. 11B). This suggests that, while the basic electrophysiological properties of PV<sup>+</sup> INs are not altered in APC cKOs, their ability to generate robust action potential firing in response to excitatory input is reduced.

### Discussion

In this study, we examined whether the development and mature function of GABAergic INs in the SSC were disrupted in the APC cKO mouse model of IESS (Fig. 12). Multiple IESS risk genes interact with APC and  $\beta$ -catenin and are important to ventral forebrain development and synaptic function (Paciorkowski et al., 2011; Pirone et al., 2017). GABAergic circuit dysfunction is thought to be a common mechanism in

multiple rodent models of IESS (Marsh et al., 2009, 2016; Price et al., 2009; Olivetti et al., 2014; Katsarou et al., 2018), may play a role in the human disorder (Bonneau et al., 2002; Kato and Dobyns, 2005), and has been reported in the adult PFC of APC cKO mice (Pirone et al., 2017). We found a transient reduction in immature PV<sup>+</sup> INs at P9, the peak age of behavioral spasms in APC cKO mice, using two different genetic reporter strategies (Figs. 1, 4). We also found that, in APC cKOs, the proportion of Cl-Casp3<sup>+</sup>/G42-GFP<sup>+</sup> INs was increased at P9 but decreased at P14; the total number of Cl-Casp3<sup>+</sup> G42-GFP<sup>+</sup> INs was also decreased at P14 (Fig. 5). This suggests that apoptosis of developing PV<sup>+</sup> INs occurs earlier in development in APC cKO than in WT animals. Whether this affects long-term circuit function or contributes to IESS-relevant phenotypes in APC cKOs is unknown, but the role of synaptic excitation of PV<sup>+</sup> IN excitation in their maturation is well documented.

At all ages examined, PV<sup>+</sup> INs receive increased spontaneous excitatory synaptic input but have decreased intrinsic excitability. At P9, PV<sup>+</sup> INs also have more elaborate dendritic morphology and receive more miniature excitatory synaptic input. Together, this suggests that enhanced excitatory-to-excitatory synaptic input, known to exist in APC cKO mice (Mohn et al., 2014; Pirone et al., 2017, 2018), drives aberrant circuit-mediated synaptic excitation of PV<sup>+</sup> INs. Only at P9, however, do PV<sup>+</sup> INs appear to have more excitatory synapses per neuron (suggested

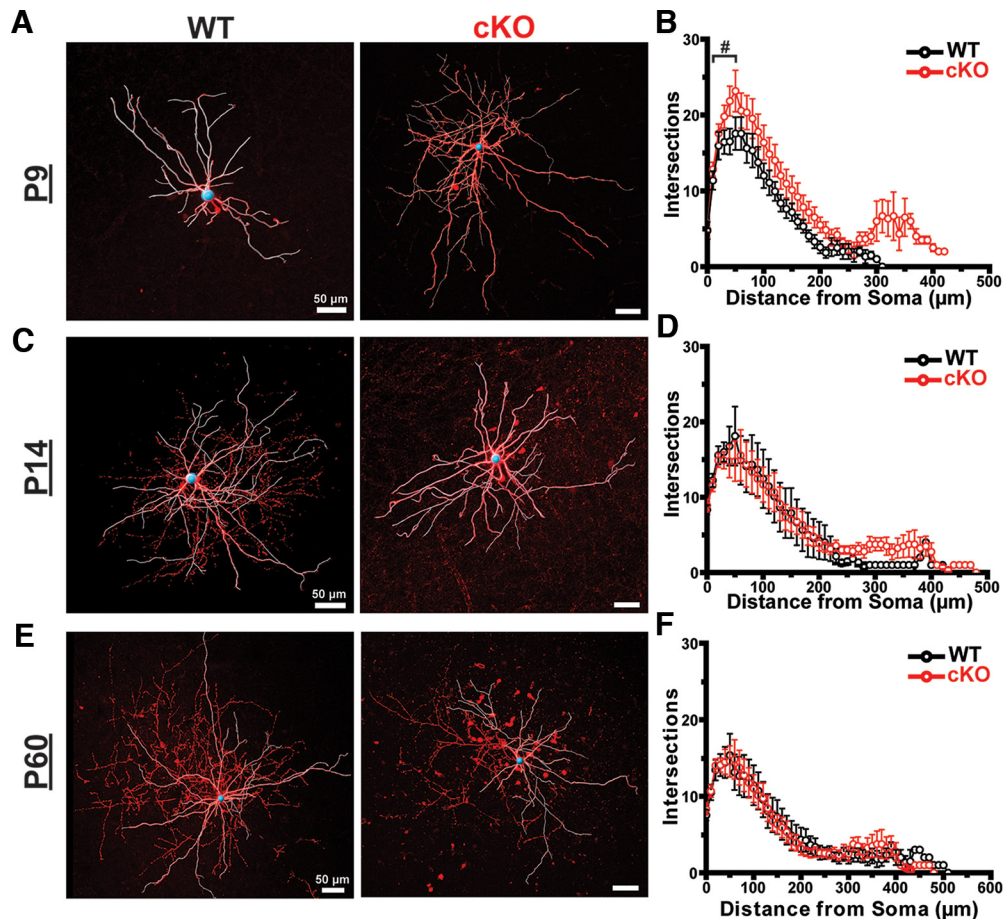


**Figure 8.** Increased dendritic complexity of P9 G42-GFP<sup>+</sup> INs in the APC cKO. **A**, Representative confocal dendritic reconstructions of biocytin-filled G42-GFP<sup>+</sup> INs from L5 SSC at P9 in WT and cKO mice. Scale bar, 50 μm. Blue sphere represents the soma. White traces represent dendrites. **B**, Scholl's analysis plot showing the number of dendritic intersections at increasing radii from the soma for biocytin-filled G42-GFP<sup>+</sup> INs at P9 in WT (black,  $n = 18$  cells, 5 animals) and cKO (red,  $n = 19$  cells, 4 animals) mice. For radii 0–60 μm,  $p = 2.25e-4$ ,  $t_{(839)} = -3.71$ , LMM. For radii 60–300 μm,  $p = 0.80$ ,  $t_{(839)} = 0.25$ , LMM. **C**, Representative confocal dendritic reconstructions of biocytin-filled G42-GFP<sup>+</sup> INs from L5 SSC at P14 in WT and cKO mice, 50 μm scale. **D**, Scholl's analysis plot showing the number of dendritic intersections at increasing radii from the soma for biocytin-filled G42-GFP<sup>+</sup> INs at P14 in WT ( $n = 14$  cells, 5 animals) and cKO ( $n = 12$  cells, 3 animals) mice. **E**, Representative confocal dendritic reconstructions of biocytin-filled G42-GFP<sup>+</sup> INs from L5 SSC at P60 in WT ( $n = 12$  cells, 3 animals) and cKO ( $n = 10$  cells, 4 animals) mice. Scale bar, 50 μm. **F**, Scholl's analysis plot showing the number of dendritic intersections at increasing radii from the soma for biocytin-filled G42-GFP<sup>+</sup> INs at P60 in WT and cKO mice. # $p < 0.05$ , LMM, effect of genotype. Each data point represents the average number of intersections per genotype. Error bars indicate SEM.

by increased mEPSC frequency), likely because of their increased dendritic arborization providing more area for excitatory synapses to form. Because PV<sup>+</sup> INs are less intrinsically excitable, however, this increased synaptic excitation does not simply increase GABAergic output of nearby L5Ps in the SSC. At P9, the age of peak behavioral spasms, GABAergic input is slightly increased (increased sIPSC amplitude and mIPSC frequency, Figs. 9, 10). But at P14, GABAergic input is significantly decreased (lower sIPSC frequency). In adult APC cKO mice, GABAergic input is again heightened (increased mIPSC/sIPSC amplitude), suggesting changes in the abundance and/or composition of GABA receptors on pyramidal neurons. GABA receptor expression is highly dynamic (Kittler and Moss, 2003; J. L. Chen et al., 2012), can be regulated by neuronal activity, and is often altered in epilepsy (Brooks-Kayal and Russek, 2012). Changes in GABA receptor composition on pyramidal neurons in the SSC may also reflect compensatory changes in response to elevated excitation in APC cKOs (Gaiarsa et al., 2002). The direct relationship between these changes in GABAergic transmission and IESS-related phenotypes is yet to be determined, but it is clear that GABAergic network maturation and function are altered in APC cKO mice.

Because activity of GABAergic INs plays such an important role in their maturation (Lin et al., 2008; Z. J. Huang, 2009; De Marco Garcia et al., 2011; Flores and Mendez, 2014), aberrant excitation of PV<sup>+</sup> INs in APC cKOs could have important long-term implications on GABAergic systems. Neuronal activity regulates PV<sup>+</sup> IN developmental apoptosis, with increased excitation of PV<sup>+</sup> INs favoring cell survival (Southwell et al., 2012; Priya et al., 2018; Wong et al., 2018). Surprisingly, developing PV<sup>+</sup> INs receive more excitatory synaptic input in APC cKOs (Figs. 6, 7) but appear to undergo earlier cell death (Fig. 5). We also show that PV<sup>+</sup> INs are less intrinsically excitable at all ages. Although PV<sup>+</sup> INs receive more synaptic excitation, they may not be more active in terms of action potential firing. Because cell survival during developmental apoptosis appears to be calcium-dependent (Southwell et al., 2012; Priya et al., 2018; Wong et al., 2018), PV<sup>+</sup> INs may undergo early apoptosis in APC cKO mice because increased synaptic excitation fails to drive increased action potential generation. Of note, at P9, the total number of Cl-Casp3<sup>+</sup>/G42-GFP is unchanged, but the ratio of G42-GFP<sup>+</sup> INs that are Cl-Casp3<sup>+</sup> is significantly increased. This suggests that there could be alterations in the generation and migration of GABAergic INs and that the ratio of Cl-

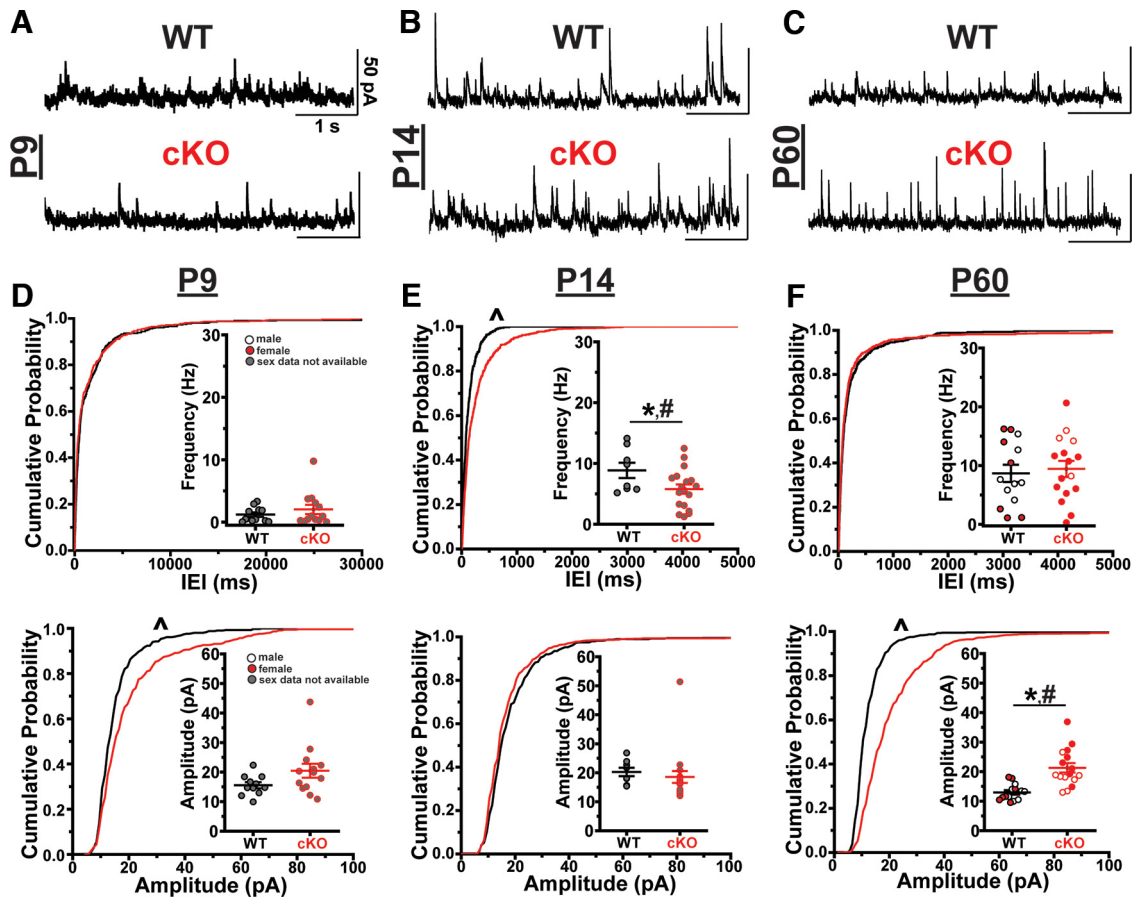


**Figure 9.** Inhibitory spontaneous output is disrupted in the cortex of APC cKO mice. Example sIPSC traces from voltage-clamped, L5 pyramidal neurons held at 0 mV at (A) P9, (B) P14, and (C) P60 for WT (black) and cKO (red) mice. All recordings made in SSC. Calibration: 50 pA, 1 s. **D**, Cumulative probability plots of IELs ( $p = 0.02$ , K-S test) with inset of mean frequency for WT (black,  $n = 11$  cells, 3 animals) and cKO (red,  $n = 13$  cells, 4 animals;  $p = 0.45$ ,  $U = 58$ , Wilcoxon rank-sum test;  $p = 0.24$ ,  $t_{(19)} = 2.57$ , LMM) and amplitude ( $p = 3.43e-7$ , K-S test) with inset of mean amplitude for WT ( $n = 11$  cells, 3 animals) and cKO ( $n = 13$  cells, 4 animals;  $p = 0.11$ ,  $U = 43$ , Wilcoxon rank-sum test;  $p = 0.07$ ,  $t_{(24)} = -1.88$ , LMM) at P9. **E**, Cumulative probability plots of IELs ( $p = 2.29e-11$ , K-S test) with inset of mean frequency for WT ( $n = 8$  cells, 3 animals) and cKO ( $n = 18$  cells, 4 animals;  $p = 0.04$ ,  $t_{(24)} = 2.16$ , two-sample  $t$  test;  $p = 0.03$ ,  $t_{(21)} = 2.41$ , LMM) and amplitude ( $p = 0.04$ , K-S test) with inset of mean amplitude for WT ( $n = 8$  cells, 3 animals) and cKO ( $n = 18$  cells, 4 animals;  $p = 0.60$ ,  $U = 44$ , Wilcoxon rank-sum test;  $p = 0.60$ ,  $t_{(21)} = 0.55$ , LMM) at P14. **F**, Cumulative probability plots of IELs ( $p = 0.21$ , K-S test) with inset of mean frequency for WT (14 cells, 4 animals) and cKO (16 cells, 6 animals;  $p = 0.71$ ,  $t_{(28)} = 0.38$ , two-sample  $t$  test;  $p = 0.85$ ,  $t_{(25)} = -0.19$ , LMM) and amplitude ( $p = 4.84e-47$ , K-S test) with inset of mean amplitude for WT ( $n = 14$  cells, 4 animals) and cKO ( $n = 16$  cells, 6 animals;  $p = 1.03e-4$ ,  $t_{(28)} = 4.52$ , two-sample  $t$  test;  $p = 5.38e-3$ ,  $t_{(25)} = -3.51$ , LMM) at P60.  $\wedge p < 0.00001$ , KS test. \* $p < 0.05$ , two-sample  $t$  test. # $p < 0.05$ , LMM, effect of genotype. Each data point represents one cell. Symbol interior color represents sex data. Data for inset graphs are mean  $\pm$  SEM.

Casp3<sup>+</sup>/G42-GFP<sup>+</sup> is increased in APC cKOs because of fewer cells migrating to the cortex. A few factors argue against this possibility. First, multiple studies show that CamKII $\alpha$ -Cre is not active embryonically when GABAergic INs are generated and migrate to the cortex (R. Z. Chen et al., 2001; Fan et al., 2001; Rios et al., 2001), making it unlikely that either process would be disrupted in APC cKOs. Second, G42-GFP<sup>+</sup> IN density is reduced in SSC, PFC, and motor cortex at P9 (Fig. 3), eliminating the possibility that fewer G42-GFP<sup>+</sup> INs are found in SSC because they migrate to other cortical regions. Finally, there is no change in SST<sup>+</sup> IN density in APC cKO SSC (Fig. 2), suggesting that there are not broad changes in IN migration and number, but rather subtype-specific changes in the early development of GABAergic systems, even among MGE-derived INs.

In addition to undergoing programmed cell death, PV<sup>+</sup> INs undergo significant structural and functional changes during the first weeks of development. The development of GABAergic synapses and PV<sup>+</sup> IN perisomatic inhibition relies on neuronal activity (Gabbott and Stewart, 1987; Chattopadhyaya et al., 2004). The formation of feedforward GABAergic circuits, mediated by cortical PV<sup>+</sup> INs, is also controlled by early neuronal activity

and reciprocal synaptic connections between GABAergic INs (Marques-Smith et al., 2016; Tuncdemir et al., 2016). Therefore, the changes in synaptic transmission we report in APC cKOs could induce long-term changes in circuit function. PV<sup>+</sup> IN excitability is also highly dynamic during development, with action potential firing rate increasing over the first weeks of postnatal development (Pangratz-Fuehrer and Hestrin, 2011). The development of fast-spiking properties relies on Kv3.1 potassium channels (Goldberg et al., 2005, 2011) and the ion channel composition of the axon-initial segment (Goldberg et al., 2008). We suspect that the decreased intrinsic excitability of PV<sup>+</sup> INs that we report may arise from disruption of potassium channel expression in APC cKO, as  $V_m$  and  $R_m$  are unaltered in APC cKOs and changes in firing rates occur predominantly at high rates of activity (Fig. 11). GABAergic signaling also promotes inhibitory circuit development (Z. J. Huang, 2009; Wu et al., 2012), so changes in GABAergic synaptic activity and PV<sup>+</sup> IN excitability could contribute to further changes in GABAergic function. Finally, because dendritogenesis relies on neuronal activity (Patz et al., 2004; Cohen et al., 2016), increased excitation of PV<sup>+</sup> INs may contribute to increased dendritic complexity in APC cKOs.

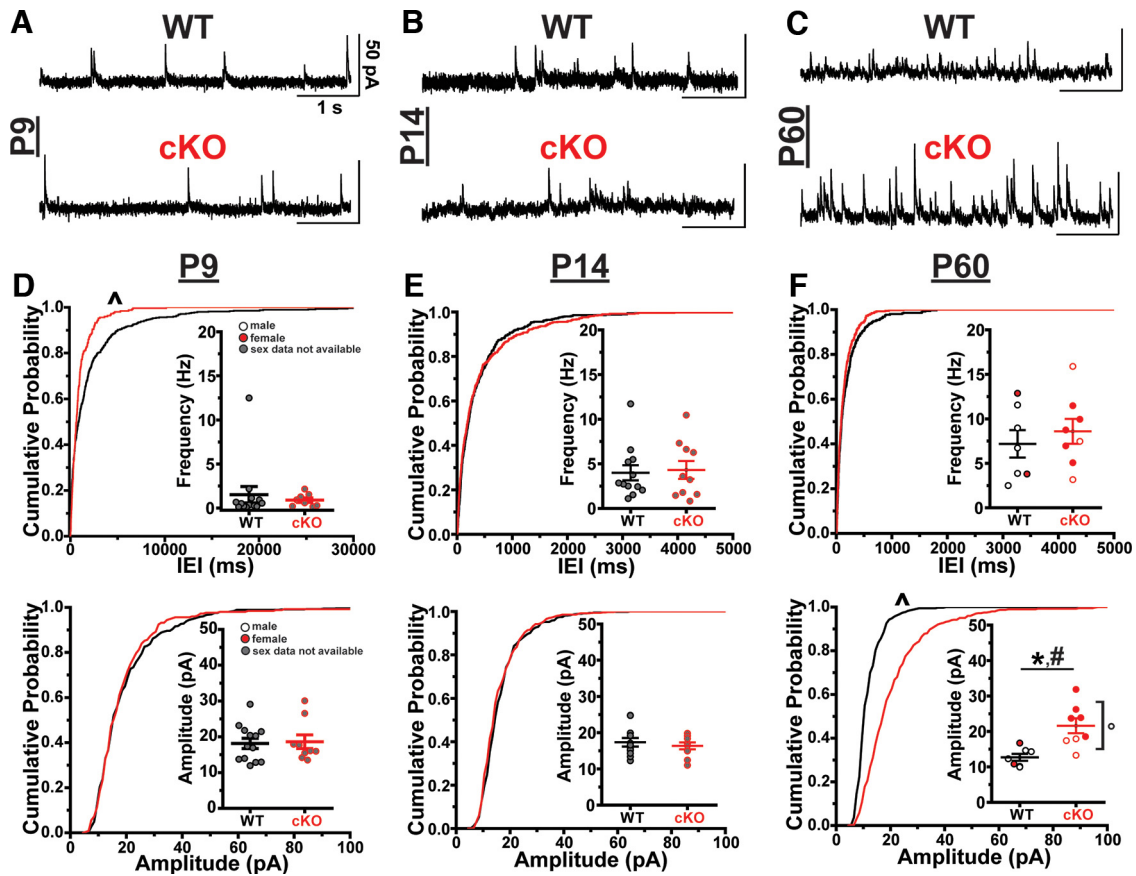


**Figure 10.** Inhibitory miniature output is disrupted in the cortex of APC cKO mice. Example mIPSC traces from voltage-clamped, L5 pyramidal neurons held at 0 mV at (A) P9, (B) P14, and (C) P60 for WT (black) and cKO (red) mice. All recordings made in SSC. Calibration: 50 pA, 1 s. **D**, Cumulative probability plots of IELs ( $p = 6.41 \times 10^{-7}$ , K-S test) with inset of mean frequency for WT (black,  $n = 13$  cells, 3 animals) and cKO (red,  $n = 8$  cells, 3 animals;  $p = 0.54$ ,  $U = 43$ , Wilcoxon rank-sum test;  $p = 0.45$ ,  $t_{(16)} = 0.83$ , LMM) and amplitude ( $p = 0.73$ , K-S test) with inset of mean amplitude for WT ( $n = 13$  cells, 3 animals) and cKO ( $n = 9$  cells, 3 animals;  $p = 0.84$ ,  $U = 55$ , Wilcoxon rank-sum test;  $p = 0.30$ ,  $t_{(17)} = -1.09$ , LMM) at P9. **E**, Cumulative probability plots of IELs ( $p = 0.11$ , K-S test) with inset of mean frequency for WT ( $n = 12$  cells, 3 animals) and cKO ( $n = 10$  cells, 3 animals;  $p = 0.92$ ,  $U = 58$ , Wilcoxon rank-sum test;  $p = 0.93$ ,  $t_{(17)} = -0.09$ , LMM) and amplitude ( $p = 0.20$ , K-S test) with inset of mean amplitude for WT ( $n = 12$  cells, 3 animals) and cKO ( $n = 10$  cells, 3 animals;  $p = 0.53$ ,  $t_{(20)} = 0.65$ , two-sample  $t$  test;  $p = 0.64$ ,  $t_{(17)} = 0.50$ , LMM) at P14. **F**, Cumulative probability plots of IELs ( $p = 0.10$ , K-S test) with inset of mean frequency for WT ( $n = 7$  cells, 3 animals) and cKO ( $n = 8$  cells, 4 animals;  $p = 0.51$ ,  $t_{(13)} = 0.68$ , two-sample  $t$  test;  $p = 0.48$ ,  $t_{(10)} = -0.73$ , LMM) and amplitude ( $p = 2.52 \times 10^{-31}$ , K-S test) with inset of mean amplitude for WT ( $n = 7$  cells, 3 animals) and cKO ( $n = 8$  cells, 4 animals;  $p = 2.85 \times 10^{-3}$ ,  $t_{(13)} = 3.67$ , two-sample  $t$  test;  $p = 0.03$ ,  $t_{(10)} = -2.79$ , LMM) at P60. Sex difference between cKO female ( $n = 5$  cells, 2 animals) and cKO male ( $n = 3$  cells, 2 animals;  $p = 0.03$ ,  $t_{(6)} = 2.82$ , two-sample  $t$  test;  $p = 2.53 \times 10^{-3}$ ,  $t_{(8)} = -3.84$ , LMM;  $p = 0.07$ ,  $t_{(8)} = 1.94$ , LMM interaction between sex and genotype) mIPSC amplitude at P60.  $\wedge p < 0.00001$ , KS test.  $*p < 0.05$ , two-sample  $t$  test.  $\#p < 0.05$ , LMM, effect of genotype.  $^{\circ}p < 0.05$ , two-sample  $t$  test and LMM, effect of sex. Each data point represents one cell. Symbol interior color represents sex data. Data for inset graphs are mean  $\pm$  SEM.

Importantly, the role of PV<sup>+</sup> INs in IESS-relevant phenotypes must be considered in the light of other changes known to occur in excitatory neurons (Mohn et al., 2014; Pirone et al., 2017) and other GABAergic INs in other brain regions (Pirone et al., 2018).

GABAergic INs are reduced in multiple models of IESS (Marsh et al., 2009, 2016; Price et al., 2009; Olivetti et al., 2014; Katsarou et al., 2018), human IESS (Bonneau et al., 2002; Kato and Dobyns, 2005), and other forms of early life epilepsy (Pancoast et al., 2005), suggesting a link between GABAergic dysfunction and early life IESS-related pathologies in APC cKO mice. Of particular note, increased GABAergic signaling at P9 (Figs. 9, 10), an age at which GABA is excitatory (Ben-Ari, 2002; Ben-Ari et al., 2007), could contribute to abnormal EEG activity and behavioral spasms. In addition, increased sIPSC/mIPSC amplitude at P60 could drive hyper-synchronization of cortical circuits or compromise GABAergic inhibition by increasing intracellular chloride levels (Deeb et al., 2013; Cohen et al., 2016), potentially contributing to seizure initiation. It is challenging, however, to directly link any of the changes we report here with IESS-relevant phenotypes in APC cKO mice.

Studies in other models of IESS also underscore the complex relationship between GABAergic signaling and IESS. For example, the changes in GABAergic INs we report here, and in other studies of the APC cKO mice, suggest unique changes in PV<sup>+</sup> and SST<sup>+</sup> INs. Interestingly, in other well-established models of IESS, namely, the multiple hit rat model (Scantlebury et al., 2010; Raffo et al., 2011; Katsarou et al., 2018), PV<sup>+</sup> INs, but not SST<sup>+</sup> or calretinin-positive GABAergic cells, are selectively lost (Katsarou et al., 2018). In the Arx expansion model of IESS, there is a decrease in calbindin-positive and neuropeptide Y GABAergic INs, but not SST<sup>+</sup>, PV<sup>+</sup>, or calretinin<sup>+</sup> INs (Price et al., 2009; Olivetti et al., 2014; Lee et al., 2017). Targeted deletion of Arx also results in a decreased density of calbindin, but not PV<sup>+</sup>, INs (Marsh et al., 2009). Interestingly, different mutations in Arx are associated with distinct changes in the density of specific GABAergic IN subpopulations (Olivetti and Noebels, 2012), adding further complexity. Of relevance to our study, there is increased apoptosis during cortical development (P7) in the Arx expansion model of IESS, although this does not occur in Arx<sup>+</sup> cells but in a non-cell-autonomous

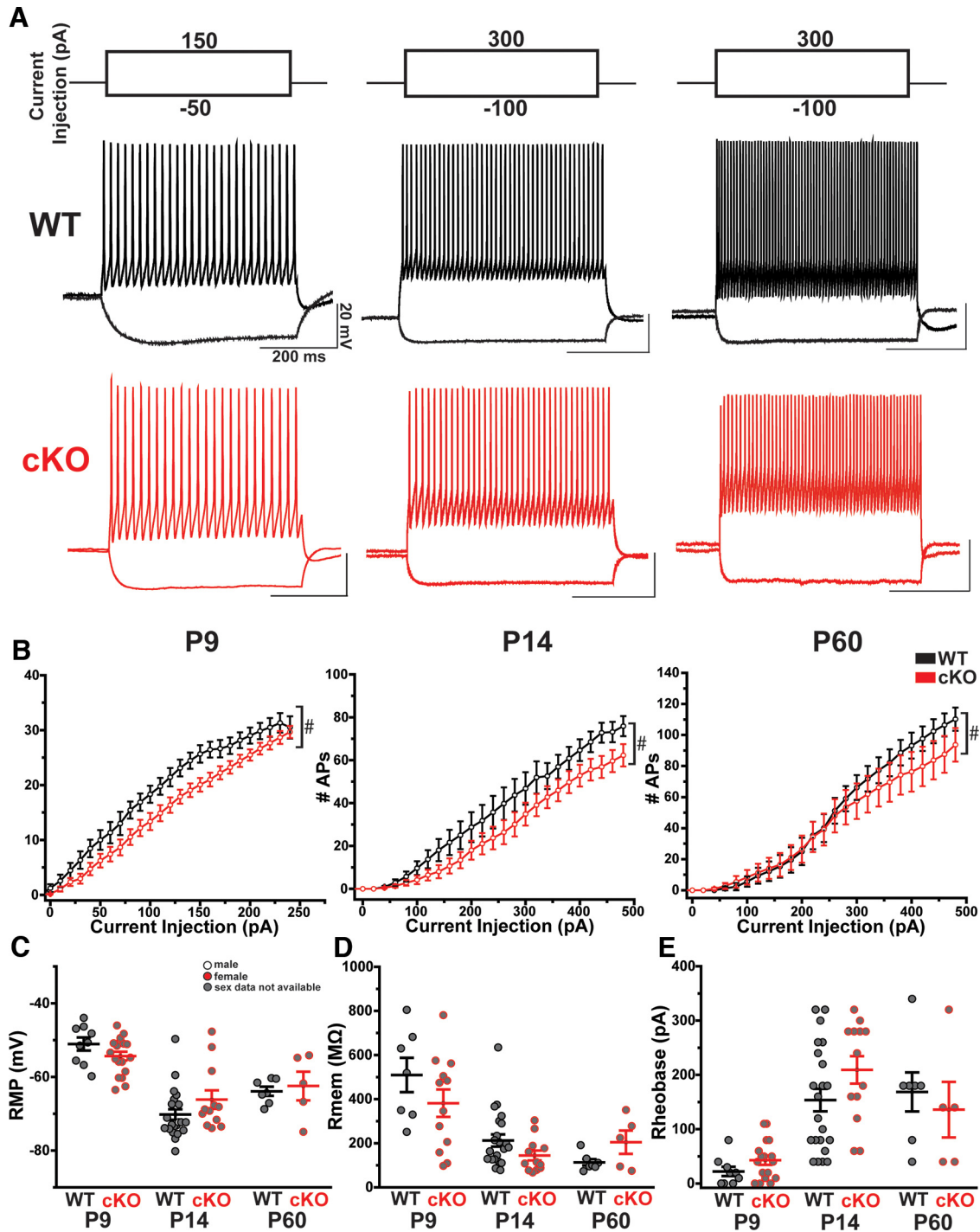


**Figure 11.** G42-GFP<sup>+</sup> INs are less intrinsically excitable in the APC cKO. **A**, Example current-clamp recordings from G42-GFP<sup>+</sup> L5 INs during hyperpolarizing and depolarizing current injections for P9, P14, and P60 in WT (black) and cKO (red) mice. All recordings made in SSC. Calibration: 20 mV, 200 ms. **B**, Graphs of the average number of action potentials (APs) generated per current injection step for WT (black) and cKO (red) mice at P9 ( $p = 2.25 \times 10^{-15}$ ,  $t_{(1014)} = 8.06$ ; LMM), P14 ( $p < 2.00 \times 10^{-16}$ ,  $t_{(2088)} = 12.2$ ; LMM), and P60 ( $p < 2.00 \times 10^{-16}$ ,  $t_{(2922)} = 8.37$ ; LMM). # $p < 0.05$ , LMM, effect of genotype. Error bars indicate SEM. **C**, Resting membrane potential (mV) between WT (black) and cKO (red) mice across ages P9, P14, and P60. **D**, Membrane resistance (MΩ) between WT (black) and cKO (red) mice across ages P9, P14, and P60. **E**, Rheobase (pA) between WT (black) and cKO (red) across ages P9, P14, and P60. Each data point represents one cell. Symbol interior color represents sex data. Data are mean  $\pm$  SEM.

fashion (Siehr et al., 2020). Because Arx signaling may share interactions with APC/ $\beta$ -catenin signaling (Cho et al., 2017; Pirone et al., 2017), it is particularly interesting that different populations of GABAergic INs are affected in each model. The molecular pathology may be completely distinct in these models, developmental differences in when dysfunction occurs (postnatal in the APC cKO and multiple-hit rat model; *in utero* in the Arx

expansion model) may contribute to model-specific changes in GABAergic INs, or unique changes in gene expression, epigenetic state, splicing, or other developmental diversification of GABAergic INs may be affected in ways we do not yet understand (Mayer et al., 2018; Wamsley et al., 2018; Allaway et al., 2021). Conversely, loss of PV<sup>+</sup> IN in both the APC cKO and multiple-hit rat model suggests that changes in PV<sup>+</sup> IN may

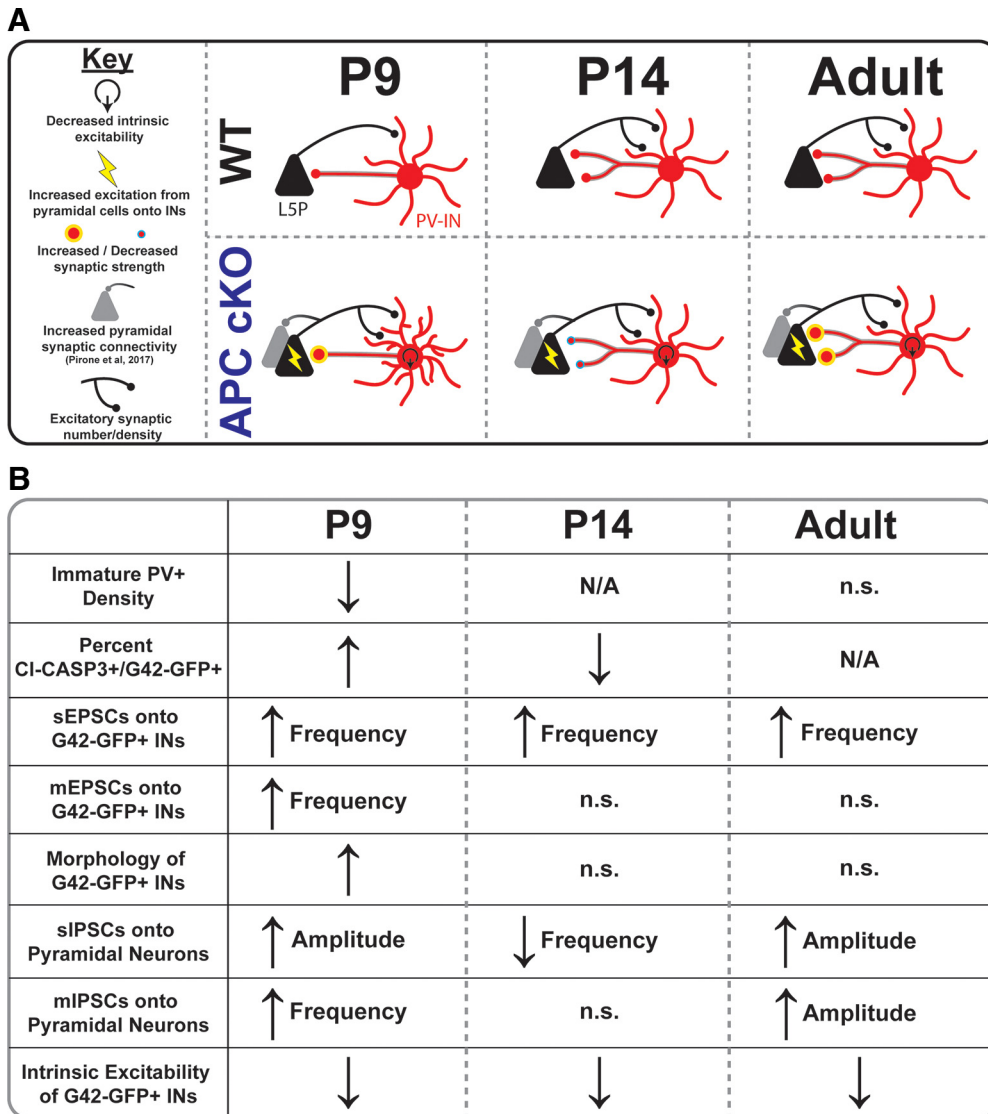


**Figure 12.** Model of synaptic and cellular changes in APC cKO somatosensory cortical inhibitory networks. **A**, Diagram represents synaptic changes seen in APC cKO mice. Increased/decreased synaptic strength only applies to PV-INs. **B**, Table describing all cellular and synaptic changes seen in APC cKO mice. **A, B**, Only statistically significant changes are included. For synaptic analysis, only changes that were statistically significant by LMM analysis of means and KS analysis of cumulative distributions were included. N/A, Not analyzed; n.s., not significant.

have more to do with the presence of infantile spasms, rather than a specific disruption in APC/ $\beta$ -catenin signaling. Future work will be required to elucidate the molecular mechanisms driving disruptions in GABAergic INs in IESS and how those changes contribute to disease pathology.

While our findings demonstrate disruptions in inhibitory network development and mature function in the APC cKO mouse, there are open questions and caveats that remain. First, identifying immature PV<sup>+</sup> INs at P9 is challenging because PV protein is not expressed until later in life. To increase rigor, we have two genetic reporter lines (G42 and Lhx6-GFP) to quantify immature PV<sup>+</sup> IN density. Novel viral approaches (Dimidschstein et al., 2016; Vormstein-Schneider et al., 2020) and advances in our molecular understanding of PV<sup>+</sup> IN maturation (Fishell, 2007; Karayannis et al., 2014; Mayer et al., 2018; Allaway et al., 2021) may enhance our ability to identify and manipulate immature PV<sup>+</sup> INs with increased confidence. Second, we do not find that decreases in PV<sup>+</sup> IN density persist into adulthood in the SSC. We suspect this may be brain region-specific, as we have previously shown decreases in both PV<sup>+</sup> and SST<sup>+</sup> IN densities in the

PFC of adult cKO mice (Pirone et al., 2018). Third, there is increased variability in G42-GFP<sup>+</sup> IN and PV<sup>+</sup> IN cell density in APC cKO mice compared with WT littermates. This is not entirely surprising as there is significant heterogeneity of behavioral spasms and seizures in APC cKOs (Pirone et al., 2017). Whether the variability in GABAergic IN density is related to heterogeneity in IESS-relevant phenotypes remains to be seen. Variability in reporter expression may also contribute as GFP<sup>+</sup> expression in G42 cells increases over the second postnatal week (Chattopadhyaya et al., 2004), the same time window in which we measure IN densities. Again, use of the Lhx6-GFP<sup>+</sup> reporter, which has more stable GFP expression in early development, helps mitigate this concern. Fourth, we do not address whether altered Wnt/ $\beta$ -catenin signaling in excitatory neurons leads to non-cell-autonomous effects in nearby PV<sup>+</sup> INs, including changes in IN proliferation and/or migration. Although Wnt/ $\beta$ -catenin signaling affects IN proliferation and cell fate decisions (Backman et al., 2005; Gulacsi and Anderson, 2008; Paina et al., 2011; Allaway et al., 2021), those events occur before CamKII $\alpha$ -Cre expression in APC

cKO mice (Pirone et al., 2017). Finally, this study was not designed or powered to address sex as a biological variable; and animal sex was not recorded for all experiments, especially at younger ages. Because of this, we cannot evaluate the role of sex as a biological variable across all findings. Interestingly, mIPSC amplitude, but not sIPSC amplitude, was increased in APC cKO females compared to APC cKO males. This is consistent with sex-specific changes reported in other IESS models (Marsh et al., 2009; Ono et al., 2011; Briggs et al., 2014; Olivetti et al., 2014; Dube et al., 2015; Frost et al., 2015; Gataullina et al., 2016; Siehr et al., 2020; Akman et al., 2021; Loring et al., 2021) and indicates that sex-specific changes should be investigated in future studies. No effects of sex on adult density of PV<sup>+</sup> INs, G42-GFP-INs, Lhx6-GFP<sup>+</sup> INs, or SST<sup>+</sup> INs, or any other measures of GABAergic synaptic transmission were seen. Future studies will be powered to examine sex as a biological variable on all outcomes.

Those caveats aside, determining whether IN dysfunction during early development is sufficient to drive behavioral infantile spasms and later electroclinical seizures is of great scientific and clinical interest. The evidence from human and mouse models of IESS, including the APC cKO mouse, suggest a role for IN dysfunction in IESS and implicate them in the circuit mechanisms that drive both infantile spasms and adult seizures. Our work points to P9 as a pivotal developmental time point in the APC cKO mouse, with peak behavioral spasms (Pirone et al., 2017) coinciding with decreased PV<sup>+</sup> IN density, an increased proportion of cell death in G42-GFP<sup>+</sup> INs, increased glutamatergic input, and increased dendritic complexity of PV<sup>+</sup> INs. In addition, this highlights a critical window during the second postnatal week for inhibitory circuit integration, in which feedback and feedforward inhibition are the ultimate outcome in normal development (Gabernet et al., 2005; Cruikshank et al., 2007; Lim et al., 2018). Disruption in neuronal activity, ambient glutamate levels, and IN maturation during this time window can lead to long-term changes in circuit structure and function (Andresen et al., 2014; Tuncdemir et al., 2016; Lau et al., 2017; Hanson et al., 2019) and may contribute to IESS-relevant phenotypes. Finally, our findings show that excitatory neuron dysfunction can initiate long-term IN dysfunction and further implicate GABAergic dysfunction in IESS, even when pathology is initiated in other neuronal types. They also underscore the importance of clinical efforts to identify patients with IESS very early in life for therapeutic intervention (Shields, 2006).

In conclusion, our findings show that PV<sup>+</sup> INs and cortical inhibitory networks are disrupted during early development in APC cKO mice and suggest that this may contribute to the manifestation of spasms and later seizures.

## References

- Aarts E, Verhage M, Veenvliet JV, Dolan CV, van der Sluis S (2014) A solution to dependency: using multilevel analysis to accommodate nested data. *Nat Neurosci* 17:491–496.
- Akman O, Briggs SW, Mowrey WB, Moshe SL, Galanopoulou AS (2021) Antiepileptogenic effects of rapamycin in a model of infantile spasms due to structural lesions. *Epilepsia* 62:1985–1999.
- Alexander JM, Pirone A, Jacob MH (2020) Excessive beta-catenin in excitatory neurons results in reduced social and increased repetitive behaviors and altered expression of multiple genes linked to human autism. *Front Synaptic Neurosci* 12:14.
- Allaway KC, Gabitto MI, Wapinski O, Saldi G, Wang CY, Bandler RC, Wu SJ, Bonneau R, Fishell G (2021) Genetic and epigenetic coordination of cortical interneuron development. *Nature* 597:693–697.
- Alroy J, et al. (2008) Phanerozoic trends in the global diversity of marine invertebrates. *Science* 321:97–100.
- Andresen L, Hampton D, Taylor-Weiner A, Morel L, Yang Y, Maguire J, Dulla CG (2014) Gabapentin attenuates hyperexcitability in the freeze-lesion model of developmental cortical malformation. *Neurobiol Dis* 71:305–316.
- Backman M, Machon O, Mygland L, van den Bout CJ, Zhong W, Taketo MM, Krauss S (2005) Effects of canonical Wnt signaling on dorso-ventral specification of the mouse telencephalon. *Dev Biol* 279:155–168.
- Bamji SX, Shimazu K, Kimes N, Huelsken J, Birchmeier W, Lu B, Reichardt LF (2003) Role of beta-catenin in synaptic vesicle localization and presynaptic assembly. *Neuron* 40:719–731.
- Behrens J, von Kries JP, Kuhl M, Bruhn L, Wedlich D, Grosschedl R, Birchmeier W (1996) Functional interaction of beta-catenin with the transcription factor LEF-1. *Nature* 382:638–642.
- Ben-Ari Y (2002) Excitatory actions of GABA during development: the nature of the nurture. *Nat Rev Neurosci* 3:728–739.
- Ben-Ari Y, Gaiarsa JL, Tyzio R, Khazipov R (2007) GABA: a pioneer transmitter that excites immature neurons and generates primitive oscillations. *Physiol Rev* 87:1215–1284.
- Boisgontier MP, Cheval B (2016) The ANOVA to mixed model transition. *Neurosci Biobehav Rev* 68:1004–1005.
- Bonneau D, Toutain A, Laquerriere A, Marret S, Saugier-Verber P, Barthez MA, Radi S, Biran-Mucignat V, Rodriguez D, Gelot A (2002) X-linked lissencephaly with absent corpus callosum and ambiguous genitalia (XLAG): clinical, magnetic resonance imaging, and neuropathological findings. *Ann Neurol* 51:340–349.
- Boutry-Kryza N, Labalme A, Ville D, de Bellescize J, Touraine R, Prieur F, Dimassi S, Poulat AL, Till M, Rossi M, Bourel-Ponchel E, Delignieres A, Le Moing AG, Rivier C, des Portes V, Edery P, Calender A, Sanlaville D, Lesca G (2015) Molecular characterization of a cohort of 73 patients with infantile spasms syndrome. *Eur J Med Genet* 58:51–58.
- Briggs SW, Mowrey W, Hall CB, Galanopoulou AS (2014) CPP-115, a vigabatrin analogue, decreases spasms in the multiple-hit rat model of infantile spasms. *Epilepsia* 55:94–102.
- Brooks-Kayal AR, Russek SJ (2012) Regulation of GABA<sub>A</sub> receptor gene expression and epilepsy. In: Jasper's basic mechanisms of the epilepsies (Noebels JL, Avoli M, Rogawski MA, Olsen RW, Delgado-Escueta AV, eds). Bethesda, MD: National Center for Biotechnology Information (US).
- Buzsáki G (2006) Rhythms of the brain. Oxford: Oxford UP.
- Cantu D, Walker K, Andresen L, Taylor-Weiner A, Hampton D, Tesco G, Dulla CG (2015) Traumatic brain injury increases cortical glutamate network activity by compromising GABAergic control. *Cereb Cortex* 25:2306–2320.
- Carson RP, Fu C, Winzenburger P, Ess KC (2013) Deletion of Rictor in neural progenitor cells reveals contributions of mTORC2 signaling to tuberous sclerosis complex. *Hum Mol Genet* 22:140–152.
- Chattopadhyaya B, Cristo GD, Higashiyama H, Knott GW, Kuhlman SJ, Welker E, Huang ZJ (2004) Experience and activity-dependent maturation of perisomatic GABAergic innervation in primary visual cortex during a postnatal critical period. *J Neurosci* 24:9598–9611.
- Chen JL, Villa KL, Cha JW, So PT, Kubota Y, Nedivi E (2012) Clustered dynamics of inhibitory synapses and dendritic spines in the adult neocortex. *Neuron* 74:361–373.
- Chen RZ, Akbarian S, Tudor M, Jaenisch R (2001) Deficiency of methyl-CpG binding protein-2 in CNS neurons results in a Rett-like phenotype in mice. *Nat Genet* 27:327–331.
- Cho IT, Lim Y, Golden JA, Cho G (2017) Aristaless Related Homeobox (ARX) Interacts with beta-catenin, BCL9, and P300 to regulate canonical Wnt signaling. *PLoS One* 12:e0170282.
- Close J, Xu H, Garcia ND, Batista-Brito R, Rossignol E, Rudy B, Fishell G (2012) Satb1 is an activity-modulated transcription factor required for the terminal differentiation and connectivity of medial ganglionic eminence-derived cortical interneurons. *J Neurosci* 32:17690–17705.
- Cohen SM, Ma H, Kuchibhotla KV, Watson BO, Buzsáki G, Froemke RC, Tsien RW (2016) Excitation-transcription coupling in parvalbumin-positive interneurons employs a novel CaM kinase-dependent pathway distinct from excitatory neurons. *Neuron* 90:292–307.
- Colombo E, Galli R, Cossu G, Geicz J, Broccoli V (2004) Mouse orthologue of ARX, a gene mutated in several X-linked forms of mental retardation and epilepsy, is a marker of adult neural stem cells and forebrain GABAergic neurons. *Dev Dyn* 231:631–639.

- Cotter D, Kerwin R, al-Sarraj S, Brion JP, Chadwick A, Lovestone S, Anderton B, Everall I (1998) Abnormalities of Wnt signalling in schizophrenia—evidence for neurodevelopmental abnormality. *Neuroreport* 9:1379–1383.
- Cruikshank SJ, Lewis TJ, Connors BW (2007) Synaptic basis for intense thalamocortical activation of feedforward inhibitory cells in neocortex. *Nat Neurosci* 10:462–468.
- Danesin C, Peres JN, Johansson M, Snowden V, Cording A, Papalopulu N, Houart C (2009) Integration of telencephalic Wnt and hedgehog signaling center activities by Foxg1. *Dev Cell* 16:576–587.
- de Lecea L, del Rio JA, Soriano E (1995) Developmental expression of parvalbumin mRNA in the cerebral cortex and hippocampus of the rat. *Brain Res Mol Brain Res* 32:1–13.
- De Marco Garcia NV, Karayannis T, Fishell G (2011) Neuronal activity is required for the development of specific cortical interneuron subtypes. *Nature* 472:351–355.
- Deeb TZ, Nakamura Y, Frost GD, Davies PA, Moss SJ (2013) Disrupted Cl(-) homeostasis contributes to reductions in the inhibitory efficacy of diazepam during hyperexcited states. *Eur J Neurosci* 38:2453–2467.
- Denaxa M, Neves G, Rabinowitz A, Kemlo S, Liodis P, Burrone J, Pachnis V (2018) Modulation of apoptosis controls inhibitory interneuron number in the cortex. *Cell Rep* 22:1710–1721.
- Dimidschstein J, et al. (2016) A viral strategy for targeting and manipulating interneurons across vertebrate species. *Nat Neurosci* 19:1743–1749.
- Dube CM, Molet J, Singh-Taylor A, Ivy A, Maras PM, Baram TZ (2015) Hyper-excitability and epilepsy generated by chronic early-life stress. *Neurobiol Stress* 2:10–19.
- El Achkar CM, Spence SJ (2015) Clinical characteristics of children and young adults with co-occurring autism spectrum disorder and epilepsy. *Epilepsy Behav* 47:183–190.
- Fan G, Beard C, Chen RZ, Csankovszki G, Sun Y, Siniatia M, Biniszkiwicz D, Bates B, Lee PP, Kuhn R, Trumpff A, Poon C, Wilson CB, Jaenisch R (2001) DNA hypomethylation perturbs the function and survival of CNS neurons in postnatal animals. *J Neurosci* 21:788–797.
- Fishell G (2007) Perspectives on the developmental origins of cortical interneuron diversity. *Novartis Found Symp* 288:21–35; discussion 35–44, 96–98.
- Flores CE, Mendez P (2014) Shaping inhibition: activity dependent structural plasticity of GABAergic synapses. *Front Cell Neurosci* 8:327.
- Freund TF, Buzsáki G (1998) Interneurons of the hippocampus. *Hippocampus* 6:347–470.
- Friocourt G, Poirier K, Rakic S, Parnavelas JG, Chelly J (2006) The role of ARX in cortical development. *Eur J Neurosci* 23:869–876.
- Frost JD Jr, Le JT, Lee CL, Ballester-Rosado C, Hrachovy RA, Swann JW (2015) Vigabatrin therapy implicates neocortical high frequency oscillations in an animal model of infantile spasms. *Neurobiol Dis* 82:1–11.
- Fu C, Cawthon B, Clinkscales W, Bruce A, Winzenburger P, Ess KC (2012) GABAergic interneuron development and function is modulated by the Tsc1 gene. *Cereb Cortex* 22:2111–2119.
- Gabbott PL, Stewart MG (1987) Quantitative morphological effects of dark-rearing and light exposure on the synaptic connectivity of layer 4 in the rat visual cortex (area 17). *Exp Brain Res* 68:103–114.
- Gabernet L, Jadhav SP, Feldman DE, Carandini M, Scanziani M (2005) Somatosensory integration controlled by dynamic thalamocortical feed-forward inhibition. *Neuron* 48:315–327.
- Gaiarsa JL, Caillard O, Ben-Ari Y (2002) Long-term plasticity at GABAergic and glycinergic synapses: mechanisms and functional significance. *Trends Neurosci* 25:564–570.
- Gataullina S, Lemaire E, Wendling F, Kaminska A, Watrin F, Riquet A, Ville D, Moutard ML, de Saint Martin A, Napuri S, Pedespan JM, Eisermann M, Bahi-Buisson N, Nabbout R, Chiron C, Dulac O, Huberfeld G (2016) Epilepsy in young Tsc1(+/-) mice exhibits age-dependent expression that mimics that of human tuberous sclerosis complex. *Epilepsia* 57:648–659.
- Go CY, Mackay MT, Weiss SK, Stephens D, Adams-Webber T, Ashwal S, Snead OC 3rd, Society of Child Neurology, Neurology American Academy (2012) Evidence-based guideline update: medical treatment of infantile spasms. Report of the Guideline Development Subcommittee of the American Academy of Neurology and the Practice Committee of the Child Neurology Society. *Neurology* 78:1974–1980.
- Goldberg EM, Watanabe S, Chang SY, Joho RH, Huang ZJ, Leonard CS, Rudy B (2005) Specific functions of synaptically localized potassium channels in synaptic transmission at the neocortical GABAergic fast-spiking cell synapse. *J Neurosci* 25:5230–5235.
- Goldberg EM, Clark BD, Zagha E, Nahmani M, Erisir A, Rudy B (2008) K<sup>+</sup> channels at the axon initial segment dampen near-threshold excitability of neocortical fast-spiking GABAergic interneurons. *Neuron* 58:387–400.
- Goldberg EM, Jeong HY, Kruglikov I, Tremblay R, Lazarenko RM, Rudy B (2011) Rapid developmental maturation of neocortical FS cell intrinsic excitability. *Cereb Cortex* 21:666–682.
- Gulacsi AA, Anderson SA (2008) Beta-catenin-mediated Wnt signaling regulates neurogenesis in the ventral telencephalon. *Nat Neurosci* 11:1383–1391.
- Hanson E, Armbruster M, Cantu D, Andresen L, Taylor A, Danbolt NC, Dulla CG (2015) Astrocytic glutamate uptake is slow and does not limit neuronal NMDA receptor activation in the neonatal neocortex. *Glia* 63:1784–1796.
- Hanson E, Armbruster M, Lau LA, Sommer ME, Klafit ZJ, Swanger SA, Traynelis SF, Moss SJ, Noubary F, Chadchankar J, Dulla CG (2019) Tonic activation of GluN2C/GluN2D-containing NMDA receptors by ambient glutamate facilitates cortical interneuron maturation. *J Neurosci* 39:3611–3626.
- Hebbar S, Guillotte AM, Mesngon MT, Zhou Q, Wynshaw-Boris A, Smith DS (2008) Genetic enhancement of the Lis1<sup>+/-</sup> phenotype by a heterozygous mutation in the adenomatous polyposis coli gene. *Dev Neurosci* 30:157–170.
- Huang J, Manning BD (2008) The TSC1-TSC2 complex: a molecular switchboard controlling cell growth. *Biochem J* 412:179–190.
- Huang ZJ (2009) Activity-dependent development of inhibitory synapses and innervation pattern: role of GABA signalling and beyond. *J Physiol* 587:1881–1888.
- Ivaniutins U, Chen Y, Mason JO, Price DJ, Pratt T (2009) Adenomatous polyposis coli is required for early events in the normal growth and differentiation of the developing cerebral cortex. *Neural Dev* 4:3.
- Karayannis T, et al. (2014) Cntnap4 differentially contributes to GABAergic and dopaminergic synaptic transmission. *Nature* 511:236–240.
- Kato M, Dobyns WB (2003) Lissencephaly and the molecular basis of neuronal migration. *Hum Mol Genet* 12:R89–R96.
- Kato M, Dobyns WB (2005) X-linked lissencephaly with abnormal genitalia as a tangential migration disorder causing intractable epilepsy: proposal for a new term, 'interneuronopathy.' *J Child Neurol* 20:392–397.
- Katsarou AM, Li Q, Liu W, Moshe SL, Galanopoulou AS (2018) Acquired parvalbumin-selective interneuronopathy in the multiple-hit model of infantile spasms: a putative basis for the partial responsiveness to vigabatrin analogs? *Epilepsia Open* 3:155–164.
- Khazipov R (2016) GABAergic synchronization in epilepsy. *Cold Spring Harb Perspect Med* 6:a022764.
- Kiryushko D, Berezin V, Bock E (2004) Regulators of neurite outgrowth: role of cell adhesion molecules. *Ann NY Acad Sci* 1014:140–154.
- Kittler JT, Moss SJ (2003) Modulation of GABA<sub>A</sub> receptor activity by phosphorylation and receptor trafficking: implications for the efficacy of synaptic inhibition. *Curr Opin Neurobiol* 13:341–347.
- Klausberger T, Somogyi P (2008) Neuronal diversity and temporal dynamics: the unity of hippocampal circuit operations. *Science* 321:53–57.
- Koenig JB, Cantu D, Low C, Sommer M, Noubary F, Croker D, Whalen M, Kong D, Dulla CG (2019) Glycolytic inhibitor 2-deoxyglucose prevents cortical hyperexcitability after traumatic brain injury. *JCI Insight* 5:e126506.
- Konur S, Ghosh A (2005) Calcium signaling and the control of dendritic development. *Neuron* 46:401–405.
- Kuechler A, et al. (2015) De novo mutations in beta-catenin (CTNBN1) appear to be a frequent cause of intellectual disability: expanding the mutational and clinical spectrum. *Hum Genet* 134:97–109.
- Lau LA, Noubary F, Wang D, Dulla CG (2017)  $\alpha 2\delta$ -1 signaling drives cell death, synaptogenesis, circuit reorganization, and Gabapentin-mediated neuroprotection in a model of insult-induced cortical malformation. *eNeuro* 4:ENEURO.0316-17.2017.
- Le Magueresse C, Monyer H (2013) GABAergic interneurons shape the functional maturation of the cortex. *Neuron* 77:388–405.
- Lee K, Ireland K, Bleeze M, Shoubridge C (2017) ARX polyalanine expansion mutations lead to migration impediment in the rostral cortex coupled with a developmental deficit of calbindin-positive cortical GABAergic interneurons. *Neuroscience* 357:220–231.

- Lim L, Mi D, Llorca A, Marin O (2018) Development and functional diversification of cortical interneurons. *Neuron* 100:294–313.
- Lin Y, Bloodgood BL, Hauser JL, Lapan AD, Koon AC, Kim TK, Hu LS, Malik AN, Greenberg ME (2008) Activity-dependent regulation of inhibitory synapse development by Npas4. *Nature* 455:1198–1204.
- Liodis P, Denaxa M, Grigoriou M, Akufo-Addo C, Yanagawa Y, Pachnis V (2007) Lhx6 activity is required for the normal migration and specification of cortical interneuron subtypes. *J Neurosci* 27:3078–3089.
- Loring KE, Mattiske T, Lee K, Zysk A, Jackson MR, Noebels JL, Shoubridge C (2021) Early 17 $\beta$ -estradiol treatment reduces seizures but not abnormal behaviour in mice with expanded polyalanine tracts in the Aristaless related homeobox gene (ARX). *Neurobiol Dis* 153:105329.
- Luhmann HJ, Prince DA (1991) Postnatal maturation of the GABAergic system in rat neocortex. *J Neurophysiol* 65:247–263.
- Mak BC, Kenerson HL, Aicher LD, Barnes EA, Yeung RS (2005) Aberrant beta-catenin signaling in tuberous sclerosis. *Am J Pathol* 167:107–116.
- Marques-Smith A, Lyngholm D, Kaufmann AK, Stacey JA, Hoerder-Suabedissen A, Becker EB, Wilson MC, Molnar Z, Butt SJ (2016) A transient transaminar GABAergic interneuron circuit connects thalamocortical recipient layers in neonatal somatosensory cortex. *Neuron* 89:536–549.
- Marsh ED, Nasrallah MP, Walsh C, Murray KA, Sunnen CN, McCoy A, Golden JA (2016) Developmental interneuron subtype deficits after targeted loss of Arx. *BMC Neurosci* 17:35.
- Marsh E, Fulp C, Gomez E, Nasrallah I, Minarcik J, Sudi J, Christian SL, Mancini G, Labosky P, Dobyns W, Brooks-Kayal A, Golden JA (2009) Targeted loss of Arx results in a developmental epilepsy mouse model and recapitulates the human phenotype in heterozygous females. *Brain* 132:1563–1576.
- Mayer C, Hafemeister C, Bandler RC, Machold R, Batista Brito R, Jaglin X, Allaway K, Butler A, Fishell G, Satija R (2018) Developmental diversification of cortical inhibitory interneurons. *Nature* 555:457–462.
- McManus MF, Nasrallah IM, Pancoast MM, Wynshaw-Boris A, Golden JA (2004) Lis1 is necessary for normal non-radial migration of inhibitory interneurons. *Am J Pathol* 165:775–784.
- Michaud JL, Lachance M, Hamdan FF, Carmant L, Lortie A, Diadori P, Major P, Meijer IA, Lemyre EA, Cossette P, Mefford HC, Rouleau GA, Rossignol E (2014) The genetic landscape of infantile spasms. *Hum Mol Genet* 23:4846–4858.
- Miyoshi G, Fishell G (2012) Dynamic FoxG1 expression coordinates the integration of multipolar pyramidal neuron precursors into the cortical plate. *Neuron* 74:1045–1058.
- Mohn JL, Alexander J, Pirone A, Palka CD, Lee SY, Mebane L, Haydon PG, Jacob MH (2014) Adenomatous polyposis coli protein deletion leads to cognitive and autism-like disabilities. *Mol Psychiatry* 19:1133–1142.
- Molenaar M, van de Wetering M, Oosterwegel M, Peterson-Maduro J, Godsave S, Korinek V, Roose J, Destree O, Clevers H (1996) XTcf-3 transcription factor mediates beta-catenin-induced axis formation in *Xenopus* embryos. *Cell* 86:391–399.
- Murase S, Mosser E, Schuman EM (2002) Depolarization drives beta-catenin into neuronal spines promoting changes in synaptic structure and function. *Neuron* 35:91–105.
- Olivetti PR, Noebels JL (2012) Interneuron, interrupted: molecular pathogenesis of ARX mutations and X-linked infantile spasms. *Curr Opin Neurobiol* 22:859–865.
- Olivetti PR, Maheshwari A, Noebels JL (2014) Neonatal estradiol stimulation prevents epilepsy in Arx model of X-linked infantile spasms syndrome. *Sci Transl Med* 6:220ra12.
- Ono T, Moshe SL, Galanopoulou AS (2011) Carisbamate acutely suppresses spasms in a rat model of symptomatic infantile spasms. *Epilepsia* 52:1678–1684.
- Paciorkowski AR, Thio LL, Dobyns WB (2011) Genetic and biologic classification of infantile spasms. *Pediatr Neurol* 45:355–367.
- Paina S, Garzotto D, DeMarchis S, Marino M, Moiana A, Conti L, Cattaneo E, Perera M, Corte G, Calautti E, Merlo GR (2011) Wnt5a is a transcriptional target of Dlx homeogenes and promotes differentiation of interneuron progenitors in vitro and in vivo. *J Neurosci* 31:2675–2687.
- Pancoast M, Dobyns W, Golden JA (2005) Interneuron deficits in patients with the Miller-Dieker syndrome. *Acta Neuropathol* 109:400–404.
- Pangratz-Fuehrer S, Hestrin S (2011) Synaptogenesis of electrical and GABAergic synapses of fast-spiking inhibitory neurons in the neocortex. *J Neurosci* 31:10767–10775.
- Patz S, Grabert J, Gorba T, Wirth MJ, Wahle P (2004) Parvalbumin expression in visual cortical interneurons depends on neuronal activity and TrkB ligands during an early period of postnatal development. *Cereb Cortex* 14:342–351.
- Pavone P, Striano P, Falsaperla R, Pavone L, Ruggieri M (2014) Infantile spasms syndrome, West syndrome and related phenotypes: what we know in 2013. *Brain Dev* 36:739–751.
- Pirone A, Alexander J, Lau LA, Hampton D, Zayachkivsky A, Yee A, Yee A, Jacob MH, Dulla CG (2017) APC conditional knock-out mouse is a model of infantile spasms with elevated neuronal beta-catenin levels, neonatal spasms, and chronic seizures. *Neurobiol Dis* 98:149–157.
- Pirone A, Alexander JM, Koenig JB, Cook-Snyder DR, Palnati M, Wickham RJ, Eden L, Shrestha N, Reijmers L, Biederer T, Miczek KA, Dulla CG, Jacob MH (2018) Social stimulus causes aberrant activation of the medial prefrontal cortex in a mouse model with autism-like behaviors. *Front Synaptic Neurosci* 10:35.
- Poirier K, Van Esch H, Friocourt G, Saillour Y, Bahi N, Backer S, Souil E, Castelnaud-Ptakhine L, Beldjord C, Francis F, Bienvenu T, Chelly J (2004) Neuroanatomical distribution of ARX in brain and its localisation in GABAergic neurons. *Brain Res Mol Brain Res* 122:35–46.
- Price MG, Yoo JW, Burgess DL, Deng F, Hrachovy RA, Frost JD Jr, Noebels JL (2009) A triplet repeat expansion genetic mouse model of infantile spasms syndrome, Arx(GCG)<sup>10+7</sup>, with interneuronopathy, spasms in infancy, persistent seizures, and adult cognitive and behavioral impairment. *J Neurosci* 29:8752–8763.
- Priya R, Paredes MF, Karayannis T, Yusuf N, Liu X, Jaglin X, Graef I, Alvarez-Buylla A, Fishell G (2018) Activity regulates cell death within cortical interneurons through a calcineurin-dependent mechanism. *Cell Rep* 22:1695–1709.
- Raffo E, Coppola A, Ono T, Briggs SW, Galanopoulou AS (2011) A pulse rapamycin therapy for infantile spasms and associated cognitive decline. *Neurobiol Dis* 43:322–329.
- Riikonen R, Renner-Primec Z, Carmant L, Dorofeeva M, Hollody K, Szabo I, Krajnc BS, Wohlrab G, Sorri I (2015) Does vigabatrin treatment for infantile spasms cause visual field defects? An international multicentre study. *Dev Med Child Neurol* 57:60–67.
- Rios M, Fan G, Fekete C, Kelly J, Bates B, Kuehn R, Lechan RM, Jaenisch R (2001) Conditional deletion of brain-derived neurotrophic factor in the postnatal brain leads to obesity and hyperactivity. *Mol Endocrinol* 15:1748–1757.
- Salinas PC (2012) Wnt signaling in the vertebrate central nervous system: from axon guidance to synaptic function. *Cold Spring Harb Perspect Biol* 4:e008003.
- Scantlebury MH, Galanopoulou AS, Chudomelova L, Raffo E, Betancourth D, Moshe SL (2010) A model of symptomatic infantile spasms syndrome. *Neurobiol Dis* 37:604–612.
- Schlessinger K, Hall A, Tolwinski N (2009) Wnt signaling pathways meet Rho GTPases. *Genes Dev* 23:265–277.
- Shields WD (2006) Infantile spasms: little seizures, BIG consequences. *Epilepsy Curr* 6:63–69.
- Siehr MS, Massey CA, Noebels JL (2020) Arx expansion mutation perturbs cortical development by augmenting apoptosis without activating innate immunity in a mouse model of X-linked infantile spasms syndrome. *Dis Model Mech* 13:dmm042515.
- Solbach S, Celio MR (1991) Ontogeny of the calcium binding protein parvalbumin in the rat nervous system. *Anat Embryol (Berl)* 184:103–124.
- Southwell DG, Paredes MF, Galvao RP, Jones DL, Froemke RC, Sebe JY, Alfaro-Cervello C, Tang Y, Garcia-Verdugo JM, Rubenstein JL, Baraban SC, Alvarez-Buylla A (2012) Intrinsically determined cell death of developing cortical interneurons. *Nature* 491:109–113.
- Striano P, et al. (2011) West syndrome associated with 14q12 duplications harboring FOXG1. *Neurology* 76:1600–1602.
- Stromme P, Mangelsdorf ME, Scheffer IE, Geicz J (2002a) Infantile spasms, dystonia, and other X-linked phenotypes caused by mutations in Aristaless related homeobox gene, ARX. *Brain Dev* 24:266–268.
- Stromme P, Mangelsdorf ME, Shaw MA, Lower KM, Lewis SM, Bruyere H, Lutcheraath V, Gedeon AK, Wallace RH, Scheffer IE, Turner G, Partington M, Frints SG, Fryns JP, Sutherland GR, Mulley JC, Geicz J (2002b) Mutations in the human ortholog of Aristaless cause X-linked mental retardation and epilepsy. *Nat Genet* 30:441–445.

- Tuncdemir SN, Wamsley B, Stam FJ, Osakada F, Goulding M, Callaway EM, Rudy B, Fishell G (2016) Early somatostatin interneuron connectivity mediates the maturation of deep layer cortical circuits. *Neuron* 89:521–535.
- Vitureira N, Letellier M, White IJ, Goda Y (2012) Differential control of pre-synaptic efficacy by postsynaptic N-cadherin and beta-catenin. *Nat Neurosci* 15:81–89.
- Vormstein-Schneider D, et al. (2020) Viral manipulation of functionally distinct interneurons in mice, non-human primates and humans. *Nat Neurosci* 23:1629–1636.
- Wamsley B, Fishell G (2017) Genetic and activity-dependent mechanisms underlying interneuron diversity. *Nat Rev Neurosci* 18:299–309.
- Wamsley B, Jaglin XH, Favuzzi E, Quattrococo G, Nigro MJ, Yusuf N, Khodadadi-Jamayran A, Rudy B, Fishell G (2018) Rbfox1 mediates cell-type-specific splicing in cortical interneurons. *Neuron* 100:846–859.e7.
- West WJ (1841) On a peculiar form of infantile convulsions. *Lancet* 1:724–725.
- Wickham RJ, Alexander JM, Eden LW, Valencia-Yang M, Llamas J, Aubrey JR, Jacob MH (2019) Learning impairments and molecular changes in the brain caused by beta-catenin loss. *Hum Mol Genet* 28:2965–2975.
- Wisniewska MB, Nagalski A, Dabrowski M, Misztal K, Kuznicki J (2012) Novel beta-catenin target genes identified in thalamic neurons encode modulators of neuronal excitability. *BMC Genomics* 13:635.
- Wong FK, Bercsenyi K, Sreenivasan V, Portales A, Fernandez-Otero M, Marin O (2018) Pyramidal cell regulation of interneuron survival sculpts cortical networks. *Nature* 557:668–673.
- Wu X, Fu Y, Knott G, Lu J, Cristo GD, Huang ZJ (2012) GABA signaling promotes synapse elimination and axon pruning in developing cortical inhibitory interneurons. *J Neurosci* 32:331–343.
- Yu FH, Mantegazza M, Westenbroek RE, Robbins CA, Kalume F, Burton KA, Spain WJ, McKnight GS, Scheuer T, Catterall WA (2006) Reduced sodium current in GABAergic interneurons in a mouse model of severe myoclonic epilepsy in infancy. *Nat Neurosci* 9:1142–1149.
- Yu Z, Guindani M, Grieco SF, Chen L, Holmes TC, Xu X (2022) Beyond *t* test and ANOVA: applications of mixed-effects models for more rigorous statistical analysis in neuroscience research. *Neuron* 110:21–35.
- Zhang Z, Hartmann H, Do VM, Abramowski D, Sturchler-Pierrat C, Staufenbiel M, Sommer B, van de Wetering M, Clevers H, Saftig P, De Strooper B, He X, Yankner BA (1998) Destabilization of beta-catenin by mutations in presenilin-1 potentiates neuronal apoptosis. *Nature* 395:698–702.